Research Square

Preprints are preliminary reports that have not undergone peer review.
They should not be considered conclusive, used to inform clinical practice,
or referenced by the media as validated information.

DPI Suppression for Non-cooperative Bistatic Radar Based on Direction-Preserving Orthogonality of Signal Eigenvectors

Yiduo Guo
Air Force Engineering University
Jiawei Lu
Air Force Engineering University
Yu Zhang
zhangyu111@163.com

Air Force Engineering University

Research Article

Keywords: Direct-Path Interference (DPI), Non-cooperative bistatic radar, Direction of Arrival (DOA), Multiple Signal Classification (MUSIC)

Posted Date: September 14th, 2026

DOI: https://doi.org/10.21203/rs.3.rs-9716043/v1

License: This work is licensed under a Creative Commons Attribution 4.0 International License.
Read Full License

Additional Declarations: No competing interests reported.

DPI Suppression for Non-cooperative Bistatic Radar Based on Direction-Preserving Orthogonality of Signal Eigenvectors

Yiduo Guo [1], Jiawei Lu [1], Yu Zhang [1]

Abstract

Non-cooperative bistatic radar, which detects and tracks targets by exploiting non-cooperative illuminators of opportunity, has become a leading research focus in radar systems due to its superior survivability and cost efficiency. However, mitigating intense Direct-Path Interference (DPI) remains a critical technical for reliable target detection and tracking. In this study, we analyze the power and angular differences between DPI and target echoes, revealing that the eigenvectors corresponding to interference and targets exhibit direction-preserving orthogonality when they do not coexist within the radar main lobe across three representative scenarios. Leveraging these properties, we propose an eigenvector elimination method for DPI suppression. This approach addresses scenarios where DPI and target signals are fully coherent: it first achieves decoherence via Toeplitz matrix reconstruction, then eliminates interference eigenvectors from the signal subspace, and finally uses the remaining target-associated eigenvectors to construct the noise subspace. Target Directions of Arrival (DOA) are estimated using the subspace-based algorithms, such as Multiple Signal Classification (MUSIC) algorithm. Simulation results validate that the proposed method effectively suppresses DPI and yields more accurate DOA estimates than conventional techniques.

Keywords Direct-Path Interference (DPI) · Non-cooperative bistatic radar · Direction of Arrival (DOA) · Multiple Signal Classification (MUSIC).

1. Introduction

In recent years, non-cooperative bistatic radar detection systems have emerged as a significant area of research within the radar field, driven by the demand for more cost-effective detection methods with enhanced battlefield survivability [1]. Traditional bistatic radar systems operate with coordinated receiving and transmitting stations, relying on cooperative transmissions from the user's own side as the radiation source. In contrast, non-cooperative bistatic radar, commonly referred to as Passive Bistatic Radar (PBR) [2-4], utilizes signals emitted by third-party sources as opportunistic illuminators for passive target detection. This approach eliminates the need for a dedicated transmitting station, thereby reducing costs and further improving battlefield survivability. The inherent non-cooperative nature of external radiation sources makes their parameters uncontrollable. Currently, the most commonly used external radiation sources are primarily commercial and can be categorized as follows: First, broadcast television radiation sources, such as DVB-T [5], FM [6], and DAB [7]; second, mobile communication radiation sources, including Wi-Fi [8], GSM [9] and 5G [10]; third, satellite radiation sources for navigation and positioning, such as signals from Galileo [11], GPS [12] , and Beidou [13]. In addition to military applications, non-cooperative bistatic radar detection systems are increasingly being adopted for civilian purposes. Notably, some international electronics enthusiasts have developed Software-Defined Radio (SDR) platforms[14], which have significantly lowered the cost and increased the accessibility of small passive detection systems. In 2018, a group of electronics enthusiasts developed the Kerberos SDR platform and subsequently built a compact passive radar target detection system using this platform [15, 16] By employing DVB-T as the external radiation source, passive detection experiments were conducted on highway vehicle targets [17] and civil aircraft targets [18].

✉ Yu Zhang
zhangyu111@163.com

Yiduo Guo
guoyiduo111@126.co m

Jiawei Lu
lujiawei1001@163.com

[1] Early Warning and Detection Department, Air Force Engineering University, Xi'an, 710051, China

Non-cooperative bistatic radar presents distinct challenges compared to traditional active radar, particularly with regard to Direct-Path Interference (DPI) [19, 20]. Firstly, current non-cooperative bistatic radar systems predominantly rely on external radiation sources that are concentrated within the UHF/VHF frequency bands. This reliance results in significant multipath clutter interference within the echo channel, which often manifests as clutter originating from the surrounding environment. Secondly, the presence of strong DPI, characterized by high energy levels, can obscure target echoes, rendering them undetectable. In the absence of effective suppression of DPI, the detection of targets remains problematic. Consequently, the primary technical challenge for non-cooperative bistatic radar in achieving successful target detection lies in the suppression of both strong DPI.

Currently, the most effective and widely employed methods for addressing the aforementioned issues primarily involve spatial interference and clutter suppression, as well as temporal interference and clutter suppression. There are three principal approaches to suppression of interference and clutter within the spatial domain. The first approach is the design of a high-gain, low-sidelobe echo channel receiving antenna, which is oriented such that its null is directed towards the source of DPI, thereby facilitating physical isolation of the interference. Alternatively, the low-sidelobe weighting technique used in array antennas can be employed to suppress all interference signals that fall outside the main lobe. While this method is relatively straightforward to implement in engineering applications, its effectiveness is often limited, necessitating integration with additional filtering techniques for enhanced processing [21, 22]. The second approach is adaptive sidelobe cancellation. This technique employs multiple auxiliary antennas to capture direct waves or other multipath clutter interference signals. Subsequently, adaptive weighting is applied to the received signals to effectively cancel out both DPI and strong multipath interference signals that are in proximity to the direction of the DPI [23-25]. The third approach is adaptive beamforming. This method involves the construction of a mathematical model based on various optimization criteria to compute the optimal weighting coefficients for each element of the array, thereby achieving effective interference suppression [26, 27]. Furthermore, a Jamming Jam Method (JJM) [28], which uses the Direction of Arrival (DOA) of interference to construct a blocking matrix that mitigates these strong interferences, ultimately enhancing the Signal-to-Noise Ratio (SNR).

In the time domain, algorithms for interference and clutter suppression are primarily categorized into two groups. The first group includes adaptive Wiener filtering algorithms, commonly referred to as Least Squares (LS) algorithms. The algorithms utilized in passive radar comprise LS, Recursive Least Squares (RLS), Normalized Least Mean Squares (NLMS), Variable-Step-Size NLMS (VSSNLMS), Fast Block Least Mean Squares (FBLMS), and Total Least Squares (TLS), among others [29, 30]. The second group includes the Extensive Cancellation Algorithm (ECA), which is widely used in passive radar for clutter interference suppression due to its superior cancellation performance and favorable convergence characteristics. To enhance the efficiency of the algorithm, a batch processing-based improved version, designated as ECA Batch (ECA-B) [31], was proposed and subsequently tested and validated using a PBR experimental system operating in the VHF band. In light of the ECA-B algorithm's limitations in addressing slow-moving targets within high-dynamic clutter environments, F. Colone introduced a sliding window-based enhanced version of the algorithm, referred to as ECA-Sliding (ECA-S) [32].

Despite the contributions of the aforementioned studies, several limitations persist. One notable limitation in certain previous studies employing space-domain approaches is the assumption that the angles of interference and multipath are known [33, 34]. However, this assumption is often unpredictable in practical scenarios. Furthermore, previous studies utilizing time-domain methodologies commonly employ a Reference Channel (RC) at the receiver to capture the direct-path signal from the transmitter, along with a separate Surveillance Channel (SC) designated for collecting the target echo. These studies often operate under the assumption that the SC exclusively receives the target echo, without any contribution from the direct-path signal, and it is reasonable in many cases.

In order to address the aforementioned issues, this paper initially demonstrates, through three representative scenarios, that the corresponding eigenvectors possess direction-preserving orthogonality when both the interference and the target are not simultaneously within the range of the main-lobe. Building upon this foundation, a method utilizing eigenvector elimination is proposed to mitigate DPI. The algorithm begins with the eigenvalue decomposition of the data covariance matrix to exclude the eigenvectors associated with DPI from the signal subspace. Subsequently, the remaining eigenvectors, which correspond to the target-reflected signals, are employed to define a new signal subspace, while a noise subspace is constructed from the signal subspace. And then, the subspace-based algorithms such as Multiple Signal Classification (MUSIC), Estimating Signal Parameters via Rotational Invariance Techniques (ESPRIT) and Maximum Likelihood can be used to estimate the DOA of the target. To facilitate the demonstration of the DOA estimation results, MUSIC algorithm is utilized to estimate the DOA of the target. The detailed contributions of this paper are summarized as follows:

1) We prove that the eigenvectors corresponding to the target-reflected signals, as well as those corresponding to the DPI, exhibit direction-preserving orthogonality when the power difference between the DPI and the tar-

get-reflected signals is large, and they are not simultaneously within the main-lobe. In this paper, three typical scenarios are considered, including a DPI and a reflected signal of target, multiple DPIs and a reflected signal of target, and a DPI and multiple reflected signals of targets. It is theoretically deduced and proved that the eigenvectors have direction-preserving orthogonality, and the existence conditions of the direction-preserving orthogonality and the effectiveness of the theoretical derivation are verified through simulation experiments.

2) On the basis of proving that the signal eigenvector has the property of direction-preserving orthogonality, we propose a target DOA estimation algorithm based on eigenvector elimination, which effectively suppresses the direct-path interference. A significant advantage of this algorithm is that it does not require prior knowledge of the orientation information related to DPI, nor does it necessitate the establishment of a RC. Consequently, the proposed algorithm is straightforward to implement and entails minimal computational burden.

The remainder of this paper is structured as follows. In Section 2, we establish the signal model for non-cooperative bistatic radar and provide a brief introduction to the theoretical foundations. Section 3 examines three typical scenarios of non-cooperative bistatic radar, demonstrating that when interference and the target are not simultaneously located within the main lobe, their corresponding eigenvectors retain direction-preserving orthogonality. In Section 4, we propose an eigenvector elimination method aimed at suppressing DPI. Section 5 presents simulation and experimental results that validate the efficacy of the proposed method. Finally, Section 6 concludes the paper and discusses considerations for future research.

2. Formulation of The Problem

2.1. Problem formulation

Consider a bistatic passive radar system, as illustrated in Fig.1. The system comprises a single non-cooperative Illuminator of Opportunity (IO) and a receiving Uniform Linear Array (ULA) with L elements in spacing d. Assume that the received signals contain DPIs and the reflected signals of targets [35]. Denote that the first J signals are DPI, while the remaining M-J signals are reflected signals, and their powers and DOAs are σ_i^2, $\theta_i, i=1,2,\cdots,J,\cdots,M$ with $\sigma_1^2 > \sigma_2^2 > \cdots > \sigma_J^2 \square \ \sigma_{J+1}^2 > \cdots > \sigma_M^2$.

Therefore, the signal collected by the receiving ULA in the presence of DPI can be expressed as follows

$$x_l(t) = \sum_{i=1}^{M} s_i(t) e^{j(l-1)\pi \sin(\theta_i)} + n_l(t) \tag{1}$$

where $s_i(t)$ is the i-th unknown signal transmitted by the IO, and $n_l(t)$ is the Gaussian additive white noise at the l-th array at time t, l=1,2,$\cdots$,L. The noise is uncorrelated in both space and time, and its power is σ_n^2.

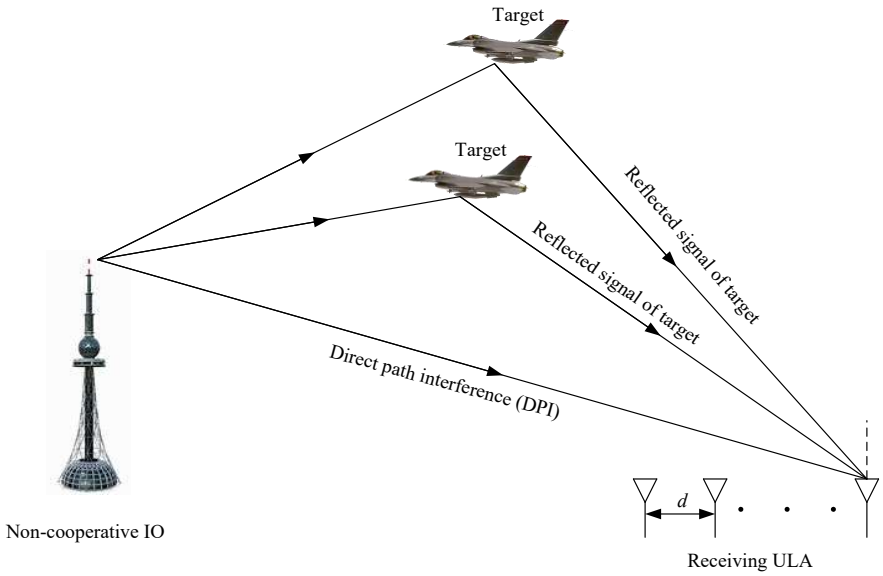


Figure 1. Geometry of bistatic passive radar system.

Its vector form can be expressed as follows

$$\boldsymbol{X}(t) = \boldsymbol{A}(\boldsymbol{\theta})\boldsymbol{S}(t) + \boldsymbol{N}(t) \tag{2}$$

where $\boldsymbol{A}(\boldsymbol{\theta})=\left[\boldsymbol{a}(\theta_1),\boldsymbol{a}(\theta_2),\cdots,\boldsymbol{a}(\theta_P)\right]$ is an $L\times P$ matrix composed of P receive steering vectors, $\boldsymbol{S}(t)=\left[\boldsymbol{s}_1(t),\boldsymbol{s}_2(t),\cdots,\boldsymbol{s}_P(t)\right]$ is the matrix consisting of amplitudes and phases of the P sources, $\boldsymbol{N}(t)=\left[\boldsymbol{n}_1(t),\boldsymbol{n}_2(t),\cdots,\boldsymbol{n}_L(t)\right]$ is the matrix of the noise, $\boldsymbol{a}(\theta_i)$ is the steering vector of the *i*-th source.

The covariance matrix $\boldsymbol{R}$ of the array signal is given by

$$\boldsymbol{R}=E\left\{\boldsymbol{X}\boldsymbol{X}^{\mathrm{H}}\right\}=\boldsymbol{A}(\boldsymbol{\theta})\boldsymbol{P}\boldsymbol{A}(\boldsymbol{\theta})^{\mathrm{H}}+\sigma_n^2\boldsymbol{I} \tag{3}$$

where $\boldsymbol{P}=E\left\{\boldsymbol{S}(t)\boldsymbol{S}^{\mathrm{H}}(t)\right\}$. If the signals are uncorrelated, $\boldsymbol{P}=diag\left\{\left[\sigma_1^2,\sigma_2^2,\cdots,\sigma_M^2\right]\right\}$.

Denote $\tilde{\boldsymbol{R}}=\boldsymbol{R}-\sigma_n^2\boldsymbol{I}$ as the signal covariance matrix, after performing the eigenvalue decomposition of $\tilde{\boldsymbol{R}}$, the following formula is derived according to the subspace theory

$$\sum_{i=1}^{M}\sigma_i^2\boldsymbol{a}(\theta_i)\boldsymbol{a}(\theta_i)^{\mathrm{H}}=\sum_{i=1}^{M}\lambda_i\boldsymbol{e}_i\boldsymbol{e}_i^{\mathrm{H}} \tag{4}$$

where $\lambda_i,\boldsymbol{e}_i\ \ i=1,2,\cdots,M$ is the large eigenvalue and corresponding eigenvector of $\tilde{\boldsymbol{R}}$. For simplicity, $\boldsymbol{a}(\theta_i)$ will be abbreviated as $\boldsymbol{a}_i$ in the following discussion.

2.2. Basic theory

The theory related to the eigenvectors of the signal correlation matrix, which is used in the subsequent analysis, is summarized below [36].

(1) Characteristic beam

The projection matrix of the steering vector $\boldsymbol{a}_i$ is $\boldsymbol{a}_i\boldsymbol{a}_i^{\mathrm{H}}/L$. The magnitude of the projection of the eigenvector $\boldsymbol{e}_j$ onto $\boldsymbol{a}_i$ can be expressed as

$$\left|\frac{\boldsymbol{a}_i\boldsymbol{a}_i^{\mathrm{H}}}{L}\boldsymbol{e}_j\right|^2=\boldsymbol{e}_j^{\mathrm{H}}\frac{\boldsymbol{a}_i\boldsymbol{a}_i^{\mathrm{H}}}{L}\frac{\boldsymbol{a}_i\boldsymbol{a}_i^{\mathrm{H}}}{L}\boldsymbol{e}_j=\frac{\left|\boldsymbol{a}_i^{\mathrm{H}}\boldsymbol{e}_j\right|^2}{L} \tag{5}$$

This means that $\left|\boldsymbol{a}_i^{\mathrm{H}}\boldsymbol{e}_j\right|^2$ can reflect the size of the projection from $\boldsymbol{e}_j$ to $\boldsymbol{a}_i$, while the characteristic beam $\left|\boldsymbol{a}^{\mathrm{H}}\boldsymbol{e}_j\right|^2$ reflects the projection of $\boldsymbol{e}_j$ on the entire array manifold. The following analysis will focus on the projection of $\boldsymbol{e}_j$ onto the steering vector and even the array manifold.

(2) The signal eigenvector $\boldsymbol{e}_j$, $j=1,2,\cdots,M$ satisfies the following equation

$$\sum_{j=1}^{M}\left|\boldsymbol{a}_i^{\mathrm{H}}\boldsymbol{e}_j\right|^2=L\quad i=1,2\cdots,M \tag{6}$$

(3) The two large non-zero eigenvalues of the data covariance matrix and their corresponding eigenvectors in the two-signal environment satisfy the following relationship

$$\begin{aligned}\lambda_1&=\frac{L\left(\sigma_1^2+\sigma_2^2\right)+\sqrt{L^2\left(\sigma_1^2-\sigma_2^2\right)^2+4\left(v\sigma_1\sigma_2\right)^2}}{2}\\ \lambda_2&=\frac{L\left(\sigma_1^2+\sigma_2^2\right)-\sqrt{L^2\left(\sigma_1^2-\sigma_2^2\right)^2+4\left(v\sigma_1\sigma_2\right)^2}}{2}\end{aligned} \tag{7}$$

$$\begin{aligned}\left|\boldsymbol{a}_1^{\mathrm{H}}\boldsymbol{e}_1\right|^2&=\frac{L}{2}+\frac{L^2\left(\sigma_1^2-\sigma_2^2\right)+2v^2\sigma_2^2}{2\sqrt{L^2\left(\sigma_1^2-\sigma_2^2\right)^2+4v^2\sigma_1^2\sigma_2^2}}\\ \left|\boldsymbol{a}_2^{\mathrm{H}}\boldsymbol{e}_2\right|^2&=\frac{L}{2}+\frac{L^2\left(\sigma_1^2-\sigma_2^2\right)-2v^2\sigma_1^2}{2\sqrt{L^2\left(\sigma_1^2-\sigma_2^2\right)^2+4v^2\sigma_1^2\sigma_2^2}}\end{aligned} \tag{8}$$

where $v=\mathrm{abs}\left(\boldsymbol{a}_1^{\mathrm{H}}\boldsymbol{a}_2\right)$.

2..3. Notation

In this paper, $(\cdot)^*$ denotes conjugate, $(\cdot)^{\mathrm{T}}$ denotes transpose, $(\cdot)^{\mathrm{H}}$ denotes conjugate transpose, $(\cdot)^{-1}$ denotes matrix inverse, $\mathrm{E}\{\cdot\}$ denotes expectation operator, $\mathrm{abs}\{\cdot\}$ denotes absolute value, $|\cdot|$ denotes module value,

$\mathrm{diag}\{\cdot\}$ denotes diagonal matrix composed of the column or row vector, $\boldsymbol{I}$ denotes identity matrix, $rank\{\cdot\}$ denotes rank of matrix, $\mathrm{toeplitz}\{\cdot\}$ denotes toeplitz matrix composed of the column or row vector.

3. Direction-Preserving Orthogonality of Signal Eigenvectors

If the eigenvector corresponding to the target reflected signal satisfies the following conditions:

1. It is maximally projected onto the guiding vector of the target-reflected signal;
2. It is orthogonal to the guiding vectors of other interference.

Then, the eigenvector of the signal is said to be direction-preserving orthogonal. In this case, the angular information of the signal emitted from each target can be extracted directly from the eigenvectors, without being affected by other interferences/clutter.

In this section, we consider the following three typical scenarios of non-cooperative bistatic radar to theoretically demonstrate that the eigenvectors corresponding to the target-reflected signals, as well as those corresponding to the DPI, exhibit direction-preserving orthogonality when the power difference between the DPI and the target-reflected signals is large, and the angles are widely separated (not simultaneously within the main-lobe).

3.1. Scenario 1: a DPI and a reflected signal of target

Assuming that the power of the DPI is σ_1^2, and the power of the reflected signal from the targets is σ_2^2, the following relationship can be obtained from Eq.7 and Eq.8 when $v=0$.

$$\lambda_1 = L\sigma_1^2, \lambda_2 = L\sigma_2^2 \tag{9}$$

Furthermore, under the additional condition that $\sigma_1^2 \neq \sigma_2^2$, the following relationship holds

$$\left|\boldsymbol{a}_1^{\mathrm{H}}\boldsymbol{e}_1\right|^2 = L,\ \left|\boldsymbol{a}_2^{\mathrm{H}}\boldsymbol{e}_2\right|^2 = L \tag{10}$$

Simultaneously, based on Equation 6, it can be derived that

$$\left|\boldsymbol{a}_1^{\mathrm{H}}\boldsymbol{e}_2\right|^2 = 0,\ \left|\boldsymbol{a}_2^{\mathrm{H}}\boldsymbol{e}_1\right|^2 = 0 \tag{11}$$

This indicates that if the steering vectors of the two signals are mutually orthogonal and their powers are unequal, the eigenvector of the signal contains directional information corresponding to that signal and remains orthogonal to the steering vectors of other signals. In other words, the eigenvector of the signal exhibits direction-preserving orthogonality.

However, the condition $v=0$ lacks practical significance, as it is only valid for a limited set of specific angles. This limitation is the primary reason for the conclusion that no correspondence exists between the signal's eigenvector and the signal itself. In reality, this conclusion is based on the assumption that the influence of signal power is negligible. When variations in signal power are considered, the direction-preserving orthogonality of the eigenvector remains valid, as demonstrated in Proposition 1.

Proposition 1. Let $\boldsymbol{a}_1$ and $\boldsymbol{e}_1$ represent the steering vector and the corresponding eigenvector of the DPI, respectively, $\boldsymbol{a}_2$ and $\boldsymbol{e}_2$ denote the steering vector and the corresponding eigenvector of the target reflected signal, respectively. When $\sigma_1^2 \gg \sigma_2^2$, the eigenvector $\boldsymbol{e}_2$ corresponding to the target reflected signal satisfies $\left|\boldsymbol{a}_2^{\mathrm{H}}\boldsymbol{e}_2\right|^2 = L - v^2/L$, $\left|\boldsymbol{a}_1^{\mathrm{H}}\boldsymbol{e}_2\right|^2 = 0$, and thus $\boldsymbol{e}_2 = \left(\left(\boldsymbol{I} - \frac{\boldsymbol{a}_1\boldsymbol{a}_1^{\mathrm{H}}}{L}\right) \Big/ \sqrt{\left(L - \frac{v^2}{L}\right)}\right)\boldsymbol{a}_2$.

Proof: See Appendix A.

From the expression of $\boldsymbol{e}_2$, it can be seen that when the DPI and the target reflected signal are not simultaneously within the main-lobe, v becomes a relatively small value, and consequently, $\left|\boldsymbol{a}_2^{\mathrm{H}}\boldsymbol{e}_2\right|^2 \approx L$. Therefore, the projection of the eigenvector corresponding to the target reflected signal onto its steering vector nearly reaches its maximum, implying that the eigenvector of the target reflected signal exhibits direction-preserving orthogonality.

3.2. Scenario 2: mltiple DPIs and a reflected signal of target

Assuming that the powers of the DPIs are much greater than that of the target reflected signal, and that the power difference between the DPIs is negligible, a precise analysis, as in Section III.A, is not feasible due to the large number of unknown conditions involved. Instead, the analysis will focus on estimating and examining the direction-preserving orthogonality of the eigenvector corresponding to the target reflected signal in this scenario.

If the first $M-1$ signals consist of DPIs, the signal covariance matrix $\tilde{\boldsymbol{R}}$ can be decomposed as follows

$$\tilde{\boldsymbol{R}} = \sum_{i=1}^{M-1} \sigma_i^2 \boldsymbol{a}_i \boldsymbol{a}_i^{\mathrm{H}} + \sigma_M^2 \boldsymbol{a}_M \boldsymbol{a}_M^{\mathrm{H}} = \tilde{\boldsymbol{R}}_{M-1} + \sigma_M^2 \boldsymbol{a}_M \boldsymbol{a}_M^{\mathrm{H}} \tag{12}$$

where $\tilde{\boldsymbol{R}}_{M-1}$ denotes the signal covariance matrix of DPIs, $\sigma_i^2 \left(i = 1, 2, \cdots, M-1\right)$ represents the power of the ith DPI, $\boldsymbol{a}_i \left(i = 1, 2, \cdots, M-1\right)$ denotes the corresponding steering vector, σ_M^2 represents the power of the target reflected signal, and $\boldsymbol{a}_M$ denotes the corresponding steering vector.

Let λ_i', $\boldsymbol{e}_i' \left(i = 1, 2, \ldots, M-1\right)$ represent the first $M-1$ eigenvalues of $\tilde{\boldsymbol{R}}_{M-1}$ and their corresponding eigenvectors, while λ_i, $\boldsymbol{e}_i$, $\left(i = 1, 2, \ldots, M-1\right)$ denote the first $M-1$ eigenvalues and their respective eigenvectors of $\tilde{\boldsymbol{R}}$. Furthermore, the following relationship holds

$$\lambda_i = \lambda_i' + \Delta\lambda_i \tag{13}$$

Given

$$\tilde{\boldsymbol{R}} \boldsymbol{e}_i = \lambda_i \boldsymbol{e}_i \quad i = 1, 2, \ldots, M-1 \tag{14}$$

While

$$\tilde{\boldsymbol{R}}_{M-1} \boldsymbol{e}_i' = \lambda_i' \boldsymbol{e}_i' \quad i = 1, 2, \ldots, M-1 \tag{15}$$

Substituting Eq.12 and Eq.13 into Eq.14, we get

$$\left(\tilde{\boldsymbol{R}}_{M-1} + \sigma_M^2 \boldsymbol{a}_M \boldsymbol{a}_M^{\mathrm{H}}\right) \boldsymbol{e}_i = \left(\lambda_i' + \Delta\lambda_i\right) \boldsymbol{e}_i \tag{16}$$

Left-multiplying both sides of Eq.17 by $\boldsymbol{e}_i'^{\mathrm{H}}$, we obtain

$$\boldsymbol{e}_i'^{\mathrm{H}} \tilde{\boldsymbol{R}}_{M-1} \boldsymbol{e}_i + \boldsymbol{e}_i'^{\mathrm{H}} \sigma_M^2 \boldsymbol{a}_M \boldsymbol{a}_M^{\mathrm{H}} \boldsymbol{e}_i = \left(\lambda_i' \boldsymbol{e}_i'^{\mathrm{H}} \boldsymbol{e}_i + \Delta\lambda_i \boldsymbol{e}_i'^{\mathrm{H}} \boldsymbol{e}_i\right) \tag{17}$$

The conjugate transpose of Eq.15 is taken and then right-multiplied by $\boldsymbol{e}_i$, resulting in the following

$$\boldsymbol{e}_i'^{\mathrm{H}} \boldsymbol{R}_{M-1} \boldsymbol{e}_i = \lambda_i' \boldsymbol{e}_i'^{\mathrm{H}} \boldsymbol{e}_i \tag{18}$$

By substituting into Eq.17, the following expression is obtained

$$\Delta\lambda_i = \sigma_M^2 \frac{\boldsymbol{e}_i'^{\mathrm{H}} \boldsymbol{a}_M \boldsymbol{a}_M^{\mathrm{H}} \boldsymbol{e}_i}{\boldsymbol{e}_i'^{\mathrm{H}} \boldsymbol{e}_i} \tag{19}$$

While

$$\sum_{i=1}^{M-1} \lambda_i' = L \sum_{i=1}^{M-1} \sigma_i^2 \tag{20}$$

$$\sum_{i=1}^{M} \lambda_i = L \sum_{i=1}^{M} \sigma_i^2 \tag{21}$$

Eq.13 is substituted into Eq.21, resulting in

$$\sum_{i=1}^{M-1} \left(\lambda_i' + \Delta\lambda_i\right) + \lambda_M = L \sum_{i=1}^{M} \sigma_i^2 \tag{22}$$

By substituting Eq.20 into Eq.22, the following is obtained

$$\lambda_M = L\sigma_M^2 - \sum_{i=1}^{M-1} \Delta\lambda_i \tag{23}$$

Finally, Eq.19 is substituted into Eq.23, yielding

$$\lambda_M = L\sigma_M^2 - \sigma_M^2 \sum_{i=1}^{M-1} \frac{\boldsymbol{e}_i'^{\mathrm{H}} \boldsymbol{a}_M \boldsymbol{a}_M^{\mathrm{H}} \boldsymbol{e}_i}{\boldsymbol{e}_i'^{\mathrm{H}} \boldsymbol{e}_i} \tag{24}$$

Proposition 2. Let $\boldsymbol{e}_M$ denote the eigenvector corresponding to the target reflected signal, and let $\boldsymbol{A}_{M-1} = \left[\boldsymbol{a}_1, \boldsymbol{a}_2, \cdots, \boldsymbol{a}_{M-1}\right]$. When $\sigma_1^2 \approx \cdots \approx \sigma_{M-1}^2 \ll \sigma_M^2$, the eigenvector $\boldsymbol{e}_M$ corresponding to the target reflected signal satisfies $\left|\boldsymbol{a}_M^{\mathrm{H}} \boldsymbol{e}_M\right|^2 = L - \sum_{i=1}^{M-1} \left|\boldsymbol{a}_M^{\mathrm{H}} \boldsymbol{e}_i\right|^2$, $\sum_{i=1}^{M-1} \sigma_i^2 \boldsymbol{a}_i \boldsymbol{a}_i^{\mathrm{H}} \boldsymbol{e}_M = 0$, and $\boldsymbol{e}_M = \dfrac{\left(\boldsymbol{I} - \boldsymbol{A}_{M-1}\left(\boldsymbol{A}_{M-1}^{\mathrm{H}} \boldsymbol{A}_{M-1}\right)^{-1} \boldsymbol{A}_{M-1}^{\mathrm{H}}\right) \boldsymbol{a}_M}{\sqrt{L - \sum_{i=1}^{M-1} \left|\boldsymbol{a}_M^{\mathrm{H}} \boldsymbol{e}_i\right|^2}}$.

Proof: See Appendix B.

When the DPIs and target reflected signal are not simultaneously located within the main-lobe, $\sum_{i=1}^{M-1} \left|\boldsymbol{a}_M^{\mathrm{H}} \boldsymbol{e}_i\right|^2$ assumes a relatively small value. In this scenario, $\left|\boldsymbol{a}_M^{\mathrm{H}} \boldsymbol{e}_M\right|^2 \approx L$.

Based on Proposition 2, it can be concluded that in the presence of multiple DPIs and one target reflected signal, the target reflected signal still exhibits direction-preserving orthogonality with respect to the DPIs.

3.3 Scenario 3: a DPI and Multiple Reflected Signals of Targets

Assuming that the power of the DPI is significantly greater than the power of the target reflected signals, the power differences among the target reflected signals are relatively small, satisfying $\sigma_1^2 \gg \sigma_2^2 \approx \cdots \approx \sigma_M^2$.

Since $\lambda_1, \lambda_2, \cdots, \lambda_M$ are the eigenvalues of $\tilde{\boldsymbol{R}}$, and they are also the eigenvalues of the following matrix $\boldsymbol{Q}$

$$\boldsymbol{Q} = \begin{bmatrix} L\sigma_1^2 & \boldsymbol{a}_1^{\mathrm{H}}\boldsymbol{a}_2\sigma_2^2 & \cdots & \boldsymbol{a}_1^{\mathrm{H}}\boldsymbol{a}_M\sigma_M^2 \\ \boldsymbol{a}_2^{\mathrm{H}}\boldsymbol{a}_1\sigma_1^2 & L\sigma_2^2 & \cdots & \boldsymbol{a}_2^{\mathrm{H}}\boldsymbol{a}_M\sigma_M^2 \\ \vdots & \vdots & \ddots & \vdots \\ \boldsymbol{a}_M^{\mathrm{H}}\boldsymbol{a}_1\sigma_1^2 & \boldsymbol{a}_M^{\mathrm{H}}\boldsymbol{a}_2\sigma_2^2 & \cdots & L\sigma_M^2 \end{bmatrix} \tag{25}$$

According to the Gershgorin circle theorem [37], the magnitude of λ_1 must satisfy

$$L\sigma_1^2 - \sum_{i=2}^{M} \boldsymbol{a}_1^{\mathrm{H}}\boldsymbol{a}_i\sigma_i^2 \le \lambda_1 \le L\sigma_1^2 + \sum_{i=2}^{M} \boldsymbol{a}_1^{\mathrm{H}}\boldsymbol{a}_i\sigma_i^2 \tag{26}$$

Eq.25 reveals the relationship between the large eigenvalues of the data covariance matrix and the power of interference and signals. Although the exact expressions for the large eigenvalues cannot be derived, their value ranges can be determined. In certain cases, the magnitudes of the large eigenvalues can be precisely determined using Eq.26.

From Eq.26, the eigenvalue λ_1 can be considered to lie within a circle on the complex plane centered at $\left(L\sigma_1^2 \quad 0\right)$. Since λ_1 is a real number, its possible values can be further confined to a symmetric region on the real axis centered at $L\sigma_1^2$. The size of this region is related to the power of signals other than s_1 and the angles between these signals and s_1. For λ_1, this region corresponds to $\sum_{i=2}^{M} \boldsymbol{a}_1^{\mathrm{H}}\boldsymbol{a}_i\sigma_i^2$, as $\sum_{i=2}^{M} \boldsymbol{a}_1^{\mathrm{H}}\boldsymbol{a}_i\sigma_i^2$ is necessarily much smaller than $\sum_{i=2}^{M} \boldsymbol{a}_i^{\mathrm{H}}\boldsymbol{a}_1\sigma_1^2$.

When $\sigma_1^2 \gg \sigma_2^2 \approx \cdots \approx \sigma_M^2$, and the angular separation between the target reflected signal and the direct wave, as well as the multipath clutter, is sufficiently large, $L >> \boldsymbol{a}_i^{\mathrm{H}}\boldsymbol{a}_j \quad i, j = 1,2,3,\cdots,M \quad i \ne j$, it leads to $L\sigma_1^2 \gg \sum_{i=2}^{M} \boldsymbol{a}_1^{\mathrm{H}}\boldsymbol{a}_i\sigma_i^2$, thereby resulting in $\lambda_1 \approx L\sigma_1^2$.

Based on the relationship between eigenvalues and eigenvectors, it can be concluded that

$$\boldsymbol{R}\boldsymbol{e}_1 = \lambda_1\boldsymbol{e}_1 \tag{27}$$

Since $\boldsymbol{R} = \sum_{i=1}^{M} \sigma_i^2\boldsymbol{a}_i\boldsymbol{a}_i^{\mathrm{H}}$, substituting it along with $\lambda_1 \approx L\sigma_1^2$ into Eq.27 and dividing both sides by σ_1^2, we obtain

$$\left(\boldsymbol{a}_1\boldsymbol{a}_1^{\mathrm{H}} + \frac{\sigma_2^2}{\sigma_1^2}\boldsymbol{a}_2\boldsymbol{a}_2^{\mathrm{H}} + \cdots + \frac{\sigma_M^2}{\sigma_1^2}\boldsymbol{a}_M\boldsymbol{a}_M^{\mathrm{H}}\right)\boldsymbol{e}_1 = L\boldsymbol{e}_1 \tag{28}$$

Since $\frac{\sigma_2^2}{\sigma_1^2}, \cdots, \frac{\sigma_M^2}{\sigma_1^2} \to 0$, it can be concluded that $\boldsymbol{a}_1\boldsymbol{a}_1^{\mathrm{H}}\boldsymbol{e}_1 = L\boldsymbol{e}_1$.

Therefore, it can be deduced that

$$\boldsymbol{e}_1 = \frac{\boldsymbol{a}_1}{\sqrt{L}} \tag{29}$$

Substituting the expression for $\boldsymbol{e}_1$ yields $\left|\boldsymbol{a}_i^{\mathrm{H}}\boldsymbol{e}_1\right|^2 = \left|\boldsymbol{a}_i^{\mathrm{H}}\boldsymbol{a}_1\right|^2 / L$. When DPI and target reflected signals do not fall simultaneously within the main-lobe, $\left|\boldsymbol{a}_i^{\mathrm{H}}\boldsymbol{a}_1\right|^2$ is a relatively small value, resulting in $\left|\boldsymbol{a}_i^{\mathrm{H}}\boldsymbol{e}_1\right|^2 \approx 0, i = 2,\cdots,M$. Therefore, it can be concluded that in the presence of DPI and multiple reflected signals of targets, DPI exhibits direction-preserving orthogonality with respect to the reflected signals.

4. Eigenvector Elimination Algorithm for Direct-Path Interference Suppression

4.1. Algorithm description

Since the DPIs and target reflected signals may be correlated or even coherent, for the convenience of analysis, the worst-case scenario is considered, where all received signals are fully coherent. In this case, $rank(\boldsymbol{P}) = 1$, and the eigenvalue decomposition of the data covariance matrix reveals that the number of dominant eigenvalues is 1, with the corresponding signal subspace having an eigenvector dimensionality of 1. Therefore, to ensure $rank(\boldsymbol{P}) = M$, it is necessary to decorrelate all signal sources.

Based on the established signal model of non-cooperative bistatic radar, for fully coherent DPIs and target reflected signals, the source covariance matrix can be expressed in terms of the signal power as

$$\boldsymbol{P}=\begin{bmatrix} \sigma_1^2 & \sigma_1\sigma_2 & \cdots & \sigma_1\sigma_J & \cdots & \sigma_1\sigma_M \\ \sigma_2\sigma_1 & \sigma_2^2 & \cdots & \sigma_2\sigma_J & \cdots & \sigma_2\sigma_M \\ \vdots & \vdots & \ddots & \vdots & \ddots & \vdots \\ \sigma_J\sigma_1 & \sigma_J\sigma_2 & \cdots & \sigma_J^2 & \cdots & \sigma_J\sigma_M \\ \vdots & \vdots & \ddots & \vdots & \ddots & \vdots \\ \sigma_M\sigma_1 & \sigma_M\sigma_2 & \cdots & \sigma_M\sigma_J & \cdots & \sigma_M^2 \end{bmatrix} \tag{30}$$

Substituting Eq.30 into Eq.4, the elements of the first row of the data covariance matrix $\boldsymbol{R}$ can be obtained as

$$\begin{cases} \boldsymbol{R}_{1,1}=\sigma_1\alpha+\cdots+\sigma_J\alpha+\cdots+\sigma_M\alpha+\sigma_n^2 \\ \boldsymbol{R}_{1,2}=\sigma_1\alpha e^{j\beta_1}+\cdots+\sigma_J\alpha e^{j\beta_J}+\cdots+\sigma_M\alpha e^{j\beta_M} \\ \qquad\vdots \\ \boldsymbol{R}_{1,L}=\sigma_1\alpha e^{j(L-1)\beta_1}+\cdots+\sigma_J\alpha e^{j(L-1)\beta_J}+\cdots+\sigma_M\alpha e^{j(L-1)\beta_M} \end{cases} \tag{31}$$

where $\boldsymbol{R}_{1,i}\left(i=1,\cdots,L\right)$ represents the *i*-th element of the first row of $\boldsymbol{R}$, and $\alpha=\left(\sigma_1+\cdots+\sigma_J+\cdots+\sigma_M\right)$.

Taking the conjugate of $\boldsymbol{R}_{1,i}\left(i=1,\cdots,L\right)$ and expressing it in vector form yields

$$\boldsymbol{V}=\begin{bmatrix} \boldsymbol{R}_{1,1}^* \\ \boldsymbol{R}_{1,2}^* \\ \vdots \\ \boldsymbol{R}_{1,L}^* \end{bmatrix}=\begin{bmatrix} 1 & \cdots & 1 & \cdots & 1 \\ e^{-j\beta_1} & \cdots & e^{-j\beta_J} & \cdots & e^{-j\beta_M} \\ \vdots & \ddots & \vdots & \ddots & \vdots \\ e^{-j(L-1)\beta_1} & \cdots & e^{-j(L-1)\beta_J} & \cdots & e^{-j(L-1)\beta_M} \end{bmatrix}\times\left[\sigma_1\alpha\cdots\sigma_J\alpha\cdots\sigma_M\alpha\right]^{\mathrm{T}}+\left[\sigma_n^2,0,\cdots,0\right]^{\mathrm{T}} \tag{32}$$

where $\boldsymbol{S}=\left[\sigma_1\alpha\ \cdots\ \sigma_J\alpha\ \cdots\ \sigma_M\alpha\right]^T$, $\boldsymbol{W}$ is an $L\times1$-dimensional vector with the first element equal to 1 and all other elements equal to 0.

A new Toeplitz matrix $\boldsymbol{R}'$ is reconstructed using $\boldsymbol{V}$

$$\boldsymbol{R}'=toeplitz\left(\boldsymbol{V}\right)=\begin{pmatrix} \boldsymbol{R}_{1,1}^* & \boldsymbol{R}_{1,2}^* & \cdots & \boldsymbol{R}_{1,L}^* \\ \boldsymbol{R}_{1,1} & \boldsymbol{R}_{1,1}^* & \cdots & \boldsymbol{R}_{1,L-1}^* \\ \vdots & \vdots & \ddots & \vdots \\ \boldsymbol{R}_{1,L} & \boldsymbol{R}_{1,L-1} & \cdots & \boldsymbol{R}_{1,1}^* \end{pmatrix}=\boldsymbol{A}\boldsymbol{P}'\boldsymbol{A}^H+\sigma_n^2\boldsymbol{I}_{L\times L} \tag{33}$$

where $\boldsymbol{P}'=\mathrm{diag}\left(\boldsymbol{S}\right)$.

From Eq.33, it can be observed that the reconstructed Toeplitz matrix $\boldsymbol{R}'$ ensures $rank\left(\boldsymbol{P}'\right)=M$, thereby achieving the decorrelation of the DPIs and target reflected signals. Consequently, the *i*-th coherent source can be treated equivalently as an independent source with a power of $\sigma_i\alpha,\left(i=1,\cdots,J,\cdots,M\right)$.

Since the first sources *J* correspond to DPIs, and their powers satisfy $\sigma_1^2>\sigma_2^2>\cdots>\sigma_J^2\ \sigma_{J+1}^2>\cdots>\sigma_M^2$, it follows that $\sigma_1\alpha>\sigma_2\alpha>\cdots>\sigma_J\alpha\ \sigma_{J+1}\alpha>\cdots>\sigma_M\alpha$. Clearly, this satisfies the condition for the direction-preserving orthogonality of the eigenvectors corresponding to the DPIs and the target reflected signals.

The eigenvalue decomposition of $\boldsymbol{R}'$ is performed, resulting in M dominant eigenvalues $\lambda_1',\lambda_2',\cdots,\lambda_J',\lambda_{J+1}',\cdots,\lambda_M'$, satisfying $\lambda_1'>\lambda_2'>\cdots>\lambda_J'\ \lambda_{J+1}'>\cdots>\lambda_M'$, with their corresponding eigenvectors $e_1',e_2',\cdots,e_J',e_{J+1}',\cdots,e_M'$. Since the eigenvectors corresponding to the DPIs and the target reflected signals exhibit direction-preserving orthogonality, the effects of the DPIs can be eliminated by removing the first J eigenvectors.

Next, the remaining $M-J$ eigenvectors are used to construct a new signal subspace $\boldsymbol{E}_S'$ corresponding to the $M-J$ target reflected signals, where $\boldsymbol{E}_S'=\left[e_{J+1}',\cdots,e_M'\right]$. The corresponding noise subspace is denoted as $\boldsymbol{E}_N'$. According to the subspace principle, $\boldsymbol{E}_N'$ satisfies

$$\boldsymbol{E}_N'\boldsymbol{E}_N'^{\mathrm{H}}=\boldsymbol{I}-\boldsymbol{E}_S'\boldsymbol{E}_S'^{\mathrm{H}} \tag{34}$$

Then, according to the MUSIC algorithm, the estimated values of the signal source's DOA are obtained as follows

$$\hat{\theta}=\arg\min_{\theta}\left\{\boldsymbol{a}^{\mathrm{H}}\left(\theta\right)\boldsymbol{E}_N'\boldsymbol{E}_N'^{\mathrm{H}}\boldsymbol{a}\left(\theta\right)\right\}=\arg\min_{\theta}\left\{\boldsymbol{a}^{\mathrm{H}}\left(\theta\right)\left(\boldsymbol{I}-\boldsymbol{E}_S'\boldsymbol{E}_S'^{\mathrm{H}}\right)\boldsymbol{a}\left(\theta\right)\right\} \tag{35}$$

The preceding analysis and discussion are based on the assumption that the total number of DPIs, denoted as J, is precisely known. However, in practical scenarios, prior knowledge of the number of DPI sources is typically unavailable. Determining the appropriate dimensionality of the subspace corresponding to the DPIs is a critical issue. If the number of dominant eigenvalues is underestimated, the suppression of DPIs will be insufficient, significantly af-

fecting the subsequent DOA estimation of the target reflected signals. Conversely, if too many dominant eigenvalues are selected, excessive cancellation of target signals may occur, leading to missed estimations of the target reflected signals. In practical applications, the number of dominant eigenvalues corresponding to the DPIs can be determined based on the variation of adjacent eigenvalues. Specifically, the number of dominant eigenvalues corresponding to the DPIs is given by *i*, which satisfies Eq.36.

$$\frac{\lambda_i}{\lambda_{i+1}} >> \frac{\lambda_{i+1}}{\lambda_{i+2}} \left(i = 1, 2, \cdots, L-2\right) \tag{36}$$

From the above analysis, it can be concluded that the larger the power of the DPIs relative to the power of the target reflected signals, the greater the corresponding eigenvalues. As the difference between the eigenvalues corresponding to the DPIs and those corresponding to the target reflected signals increases, it becomes easier to determine the dimensionality of the subspace associated with the DPIs. Thus, the DPIs are more effectively suppressed.

4.2. Algorithm steps

Based on the above analysis, the basic steps of the algorithm can be summarized as follows

(1) The data covariance matrix $\hat{\boldsymbol{R}}$ is estimated using the received array data $\boldsymbol{x}(k)$.

(2) Signal Decorrelation: The DPIs and target reflections are decorrelated using Eq.33, yielding the modified covariance matrix $\hat{\boldsymbol{R}}'$.

(3) Source Number Detection: The number of DPI sources J is determined through Eq.36.

(4) Subspace Processing: (1) Perform eigenvalue decomposition on $\hat{\boldsymbol{R}}'$ to obtain its signal subspace $\hat{\boldsymbol{E}}_S$. (2) Exclude the J dominant eigenvectors corresponding to interference components. (3) Construct the target subspace $\hat{\boldsymbol{E}}_S$ from the remaining $M-J$ eigenvectors. (4) Compute the projection matrix $\hat{\boldsymbol{E}}_N'\hat{\boldsymbol{E}}_N'^H$.

(5) The DOA estimation of the target reflected signals is achieved using Eq.35.

5. Numerical Simulations

In the simulation, it is assumed that a non-cooperative bistatic radar system is utilized, employing broadcast television signals as the external illuminator. The receiving antenna is modeled as a uniformly spaced linear array consisting of 20 elements, with the element spacing set to half a wavelength. Since the DPIs and target reflected signals are all sourced from the same radiation emitter, all signals are considered to be coherent, and the number of sources is calculated through Eq. 36. The SNR is defined as $S/N = 10\log_{10}\left(\sigma_s^2/\sigma_n^2\right)$, the Interference-to-Signal Ratio (ISR) is defined as $I/S = 10\log_{10}\left(\sigma_I^2/\sigma_s^2\right)$, and the Interference-to-Noise Ratio (INR) is defined as $I/N = 10\log_{10}\left(\sigma_I^2/\sigma_n^2\right)$, where σ_s^2 represents the signal power, σ_I^2 denotes the strong interference power, and σ_n^2 refers to the noise power.

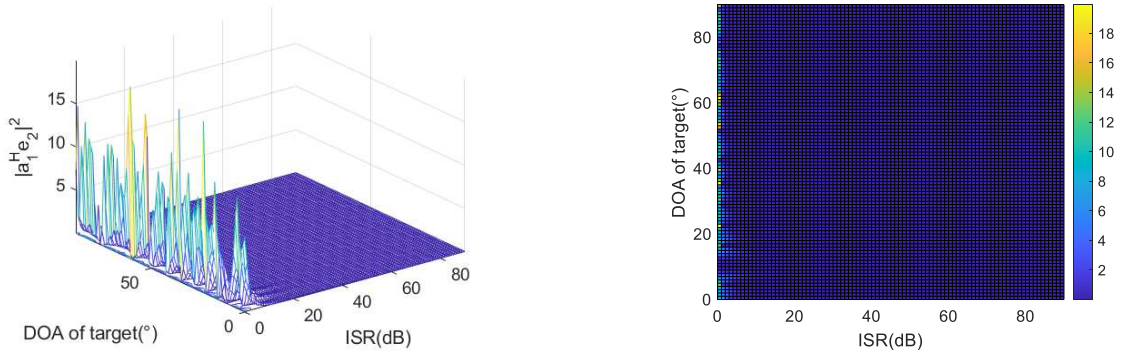
5.1. Direction-preserving orthogonality of eigenvectors corresponding to DPI and reflected signal of target

(1) A DPI and a reflected signal of target

The analysis focuses on the variation in the projection magnitude of the eigenvector associated with the target onto the steering vector, under the influence of DPI (hereinafter collectively referred to as "interference") and the target reflected signal. The interference DOA is fixed at 10°, while the DOA of the target reflected signal ranges from 0° to 90° in steps of 0.1°. The SNR is set to 0 dB, and the ISR increases from 0 dB to 90 dB in steps of 0.1 dB. Fig.2(a) and Fig.2(b) display the 3D and pseudocolor 2D plots, respectively, of the projection value $\left|\boldsymbol{a}_1\boldsymbol{e}_2^{\mathrm{H}}\right|^2$ (i.e., the projection of $\boldsymbol{e}_1$ onto $\boldsymbol{a}_1$) versus the target DOA and ISR. Similarly, Fig.3(a) and Fig.3(b) illustrate the corresponding plots for $\left|\boldsymbol{a}_2\boldsymbol{e}_2^{\mathrm{H}}\right|^2$. Here, $\boldsymbol{a}_1$ and $\boldsymbol{a}_2$ represent the steering vectors of the interference and the target reflected signal, respectively, and $\boldsymbol{e}_2$ denotes the eigenvector corresponding to the target.

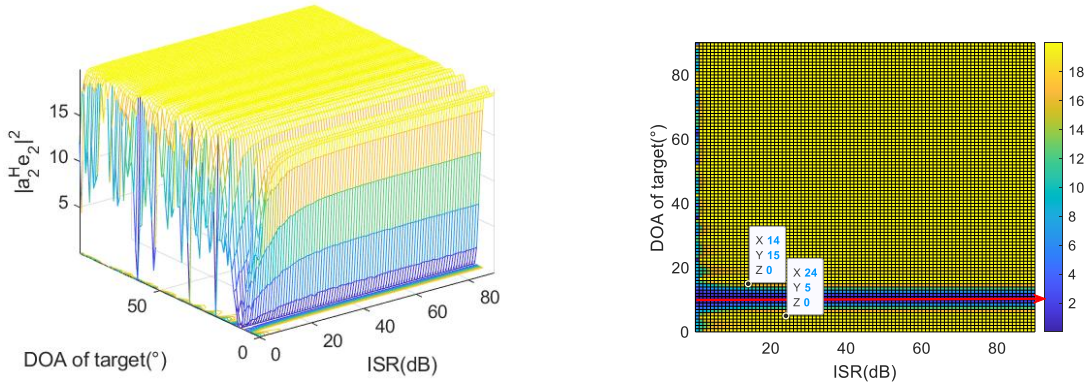
From Fig.2 and Fig.3, it can be observed that the projection value of the target eigenvector $\boldsymbol{e}_2$ onto $\boldsymbol{a}_1$ is approximately zero. Moreover, the projection value of $\boldsymbol{e}_2$ onto $\boldsymbol{a}_2$ reaches the maximum value $L=20$ for most ISR and angle conditions. It is important to note that in Fig.3, when the target angle approaches the interference angle (10°), the projection value $\left|\boldsymbol{a}_2^{\mathrm{H}}\boldsymbol{e}_2\right|^2 = L - v^2/L$ of $\boldsymbol{e}_2$ onto $\boldsymbol{a}_2$ becomes relatively small. This is because, when the beam is steered towards $\theta_0 = 10^\circ$, the main-lobe beamwidth of the radar with 20 array elements is $\frac{50.8\lambda}{Ld\cos\theta_0} \approx 5.16^\circ$. When the target angle is within the range of [5°, 10°], both the target and the interference fall within the same beam. Conse-

quently, $v = \mathrm{abs}\left(\boldsymbol{a}_1^{\mathrm{H}}\boldsymbol{a}_2\right)$ becomes relatively large, causing the projection value of $\boldsymbol{e}_2$ onto $\boldsymbol{a}_2$ to fail to reach its maximum. This does not satisfy the direction-preserving orthogonality condition of the eigenvector corresponding to the target. Hence, when there is a significant power difference between the interference and the target, and the two are not within the same beam, the eigenvector corresponding to the target exhibits direction-preserving orthogonality. The simulation results are consistent with the theoretical analysis presented in Section 3.1.



(a) (b)

Fig. 2. Variation of the projection value $\left|\boldsymbol{a}_1\boldsymbol{e}_2^{\mathrm{H}}\right|^2$ of $\boldsymbol{e}_2$ onto $\boldsymbol{a}_1$ with target DOA and ISR. (a) 3D plot. (b) 2D pseudocolor plot



(a) (b)

Fig. 3. Variation of the projection value $\left|\boldsymbol{a}_2\boldsymbol{e}_2^{\mathrm{H}}\right|^2$ of $\boldsymbol{e}_2$ onto $\boldsymbol{a}_2$ with target DOA and ISR. (a) 3D plot. (b) 2D pseudocolor plot (red arrow indicating the DOA of the interference)

(2) Multiple DPIs and a reflected rignal of target

This study investigates the variation in the projection magnitude of the eigenvector corresponding to the target reflected signal onto the steering vectors of various signals, in the presence of three DPIs and a target reflected signal. The DOAs of the DPIs are fixed at 0°, 30° and 60°, respectively. The DOA of the target reflected signal ranges from 0° to 90° in steps of 0.1°. The SNR is set to 0 dB, and the powers of the DPIs are assumed to be equal. The ISR varies from 0 dB to 90 dB in steps of 0.1 dB. To conserve space, Fig.4 provides only the pseudocolor plots illustrating the variation in the projection magnitudes of the eigenvector corresponding to the target onto the steering vectors as a function of the target DOA and ISR.

In Fig.4(a), the projection value $\left|\boldsymbol{a}_1\boldsymbol{e}_4^{\mathrm{H}}\right|^2$ of $\boldsymbol{e}_4$ onto $\boldsymbol{a}_1$ is depicted, while Fig.4(b) illustrates the projection value $\left|\boldsymbol{a}_2\boldsymbol{e}_4^{\mathrm{H}}\right|^2$ of $\boldsymbol{e}_4$ onto $\boldsymbol{a}_2$. Similarly, Fig.4(c) presents the projection value $\left|\boldsymbol{a}_3\boldsymbol{e}_4^{\mathrm{H}}\right|^2$ of $\boldsymbol{e}_4$ onto $\boldsymbol{a}_3$, and Fig.4(d) shows the projection value $\left|\boldsymbol{a}_4\boldsymbol{e}_4^{\mathrm{H}}\right|^2$ of $\boldsymbol{e}_4$ onto $\boldsymbol{a}_4$. Here, $\boldsymbol{a}_1$, $\boldsymbol{a}_2$, $\boldsymbol{a}_3$, and $\boldsymbol{a}_4$ represent the steering vectors of the three DPIs and one target reflected signal, respectively, while $\boldsymbol{e}_4$ denotes the eigenvector corresponding to the target.

Fig.4 shows that the projection values of the target eigenvector $\boldsymbol{e}_4$ onto the interference steering vectors $\boldsymbol{a}_1$, $\boldsymbol{a}_2$, and $\boldsymbol{a}_3$ are approximately zero. Additionally, when the target angle and the interference angles are not within the same beam, the projection value of $\boldsymbol{e}_4$ onto the target steering vector $\boldsymbol{a}_4$ reaches the maximum value of $L = 20$.

This indicates that the target eigenvector exhibits direction-preserving orthogonality, and the simulation results are consistent with the theoretical analysis presented in Section 3.2.

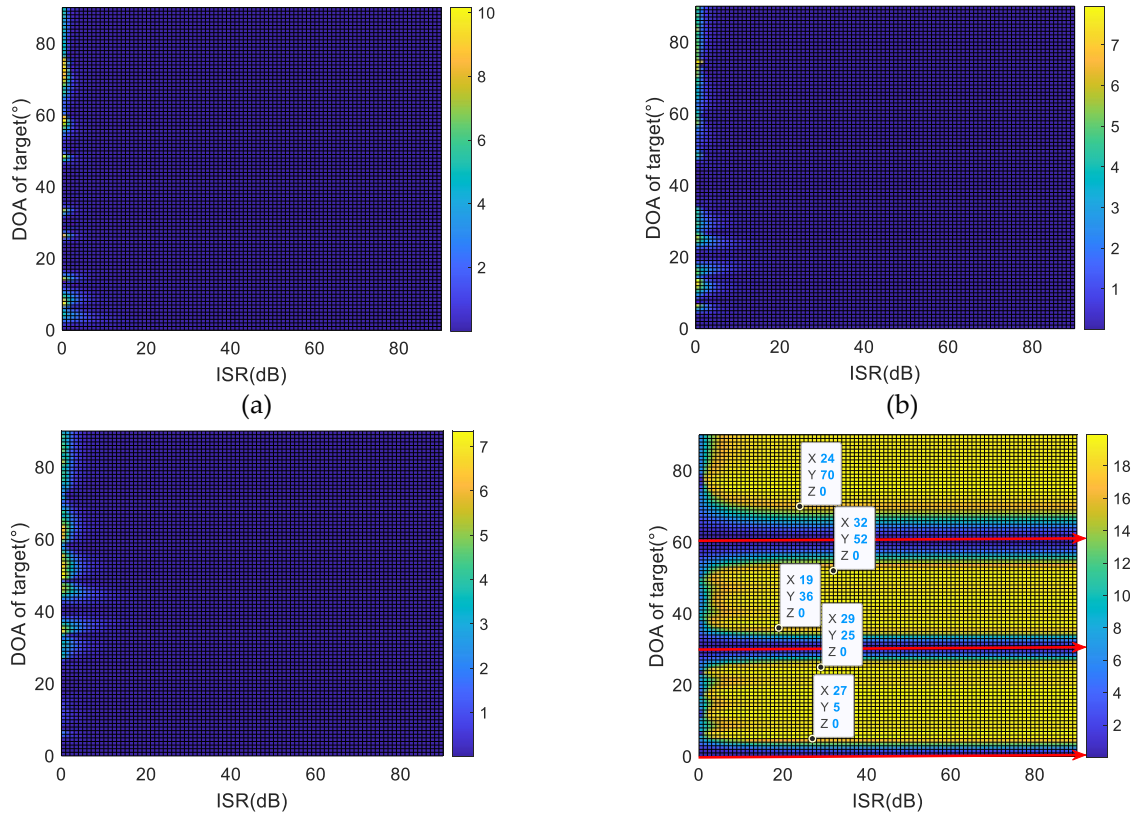


Fig. 4. Pseudocolor plots of projection magnitudes of the interference eigenvector onto steering vectors as a function of target DOA and ISR (red arrows indicate target directions). (a) Projection value $\left|\boldsymbol{a}_1\boldsymbol{e}_4^{\mathrm{H}}\right|^2$ of $\boldsymbol{e}_4$ onto $\boldsymbol{a}_1$. (b) Projection value $\left|\boldsymbol{a}_2\boldsymbol{e}_4^{\mathrm{H}}\right|^2$ of $\boldsymbol{e}_4$ onto $\boldsymbol{a}_2$. (c) Projection value $\left|\boldsymbol{a}_3\boldsymbol{e}_4^{\mathrm{H}}\right|^2$ of $\boldsymbol{e}_4$ onto $\boldsymbol{a}_3$. (d) Projection value $\left|\boldsymbol{a}_4\boldsymbol{e}_4^{\mathrm{H}}\right|^2$ of $\boldsymbol{e}_4$ onto $\boldsymbol{a}_4$.

(3) A DPI and multiple reflected signals of targets

This section considers the case of one interference signal and three target reflected signals, analyzing how the projection magnitudes of the interference's corresponding eigenvector onto the steering vectors of the target signals vary with changes in the interference's DOA and ISR. In this analysis, the azimuth angles of the three target reflected signals are fixed at 0°, 20°, and 40°, respectively, while the interference angle varies from 0° to 90° in steps of 0.1°. Additionally, it is assumed that the SNRs of all three target reflected signals are equal and set at 0 dB, and the ISR varies from 0 dB to 90 dB in steps of 0.1 dB. Fig. 5 illustrates the pseudocolor plots of the projection magnitudes of the interference eigenvector onto the steering vectors as a function of the target DOA and ISR. Specifically, Fig.5(a) shows the projection magnitude $\left|\boldsymbol{a}_1\boldsymbol{e}_1^{\mathrm{H}}\right|^2$ of $\boldsymbol{e}_1$ onto $\boldsymbol{a}_1$, Fig.5(b) shows the projection magnitude $\left|\boldsymbol{a}_2\boldsymbol{e}_1^{\mathrm{H}}\right|^2$ of $\boldsymbol{e}_1$ onto $\boldsymbol{a}_2$, Fig.5(c) shows the projection magnitude $\left|\boldsymbol{a}_3\boldsymbol{e}_1^{\mathrm{H}}\right|^2$ of $\boldsymbol{e}_1$ onto $\boldsymbol{a}_3$, and Fig.5(d) shows the projection magnitude $\left|\boldsymbol{a}_4\boldsymbol{e}_1^{\mathrm{H}}\right|^2$ of $\boldsymbol{e}_1$ onto $\boldsymbol{a}_4$. Here, $\boldsymbol{a}_1$, $\boldsymbol{a}_2$, $\boldsymbol{a}_3$, and $\boldsymbol{a}_4$ correspond to the steering vectors of one DPI and three target reflected signals, respectively, while $\boldsymbol{e}_1$ represents the eigenvector of the DPI.

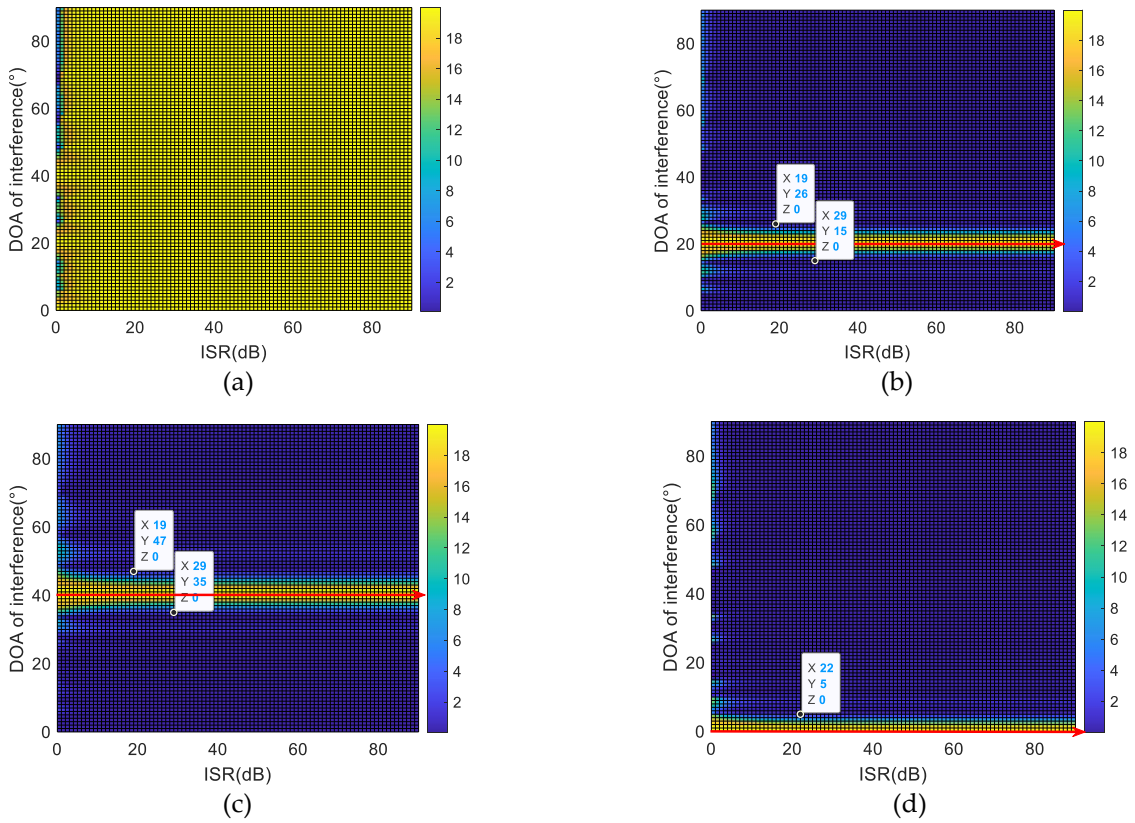


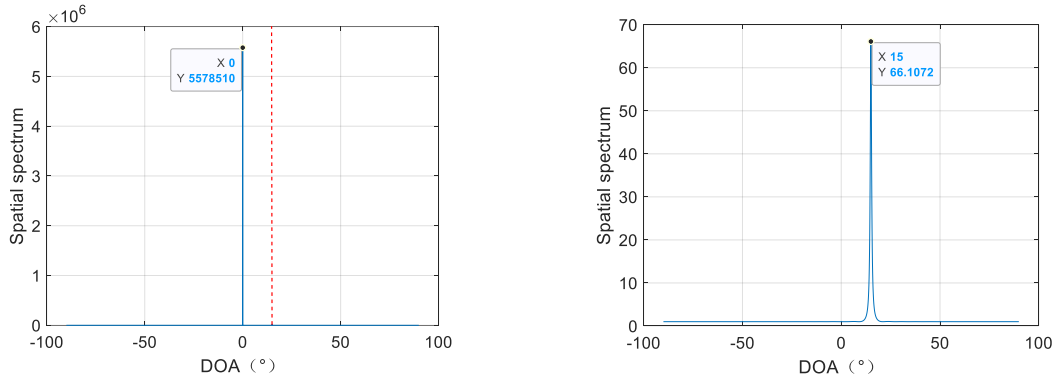
Fig. 5. Pseudocolor plots of projection magnitudes of the interference eigenvector onto steering vectors as a function of target DOA and ISR (red arrows indicate target directions). (a) Projection value $\left|\boldsymbol{a}_1\boldsymbol{e}_1^{\mathrm{H}}\right|^2$ of $\boldsymbol{e}_1$ onto $\boldsymbol{a}_1$. (b) Projection value $\left|\boldsymbol{a}_2\boldsymbol{e}_1^{\mathrm{H}}\right|^2$ of $\boldsymbol{e}_1$ onto $\boldsymbol{a}_2$. (c) Projection value $\left|\boldsymbol{a}_3\boldsymbol{e}_1^{\mathrm{H}}\right|^2$ of $\boldsymbol{e}_1$ onto $\boldsymbol{a}_3$. (d) Projection value $\left|\boldsymbol{a}_4\boldsymbol{e}_1^{\mathrm{H}}\right|^2$ of $\boldsymbol{e}_1$ onto $\boldsymbol{a}_4$.

Fig.5 demonstrates that the projection value of the interference eigenvector $\boldsymbol{e}_1$ onto the interference steering vector $\boldsymbol{a}_1$ remains consistently at its maximum, approximately L=20. When the target angles fall outside the beam range of the interference angle, the projection values of $\boldsymbol{e}_1$ onto the target steering vectors $\boldsymbol{a}_2$, $\boldsymbol{a}_3$, and $\boldsymbol{a}_4$ are nearly zero. Such results indicate that the interference eigenvector possesses direction-preserving orthogonality, with the simulation outcomes fully consistent with the theoretical analysis presented in Section 3.3.

5.2. Suppression performance of DPI

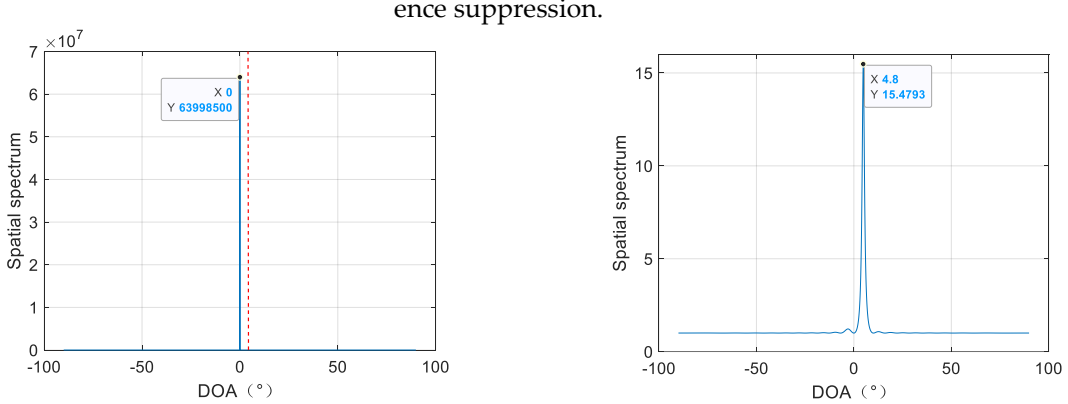
(1) A DPI and a reflected signal of target

In this analysis, it is assumed that the incident angle of the DPI is 0°, the INR is 60 dB, and the SNR is 0 dB. Fig.6 presents the spatial spectrum curves before and after interference suppression using the proposed algorithm, when the target angle is 15° (where the target and interference are not within the same beam range). Fig. 7 displays the spatial spectrum curves before and after interference suppression using the proposed algorithm when the target angle is 4° (where the target and interference are within the same beam range). The red dashed line in the figures indicates the direction of the target.



(a) (b)

Fig. 6. Target and interference located in separate beam ranges. (a) Before interference suppression. (b) After interference suppression.

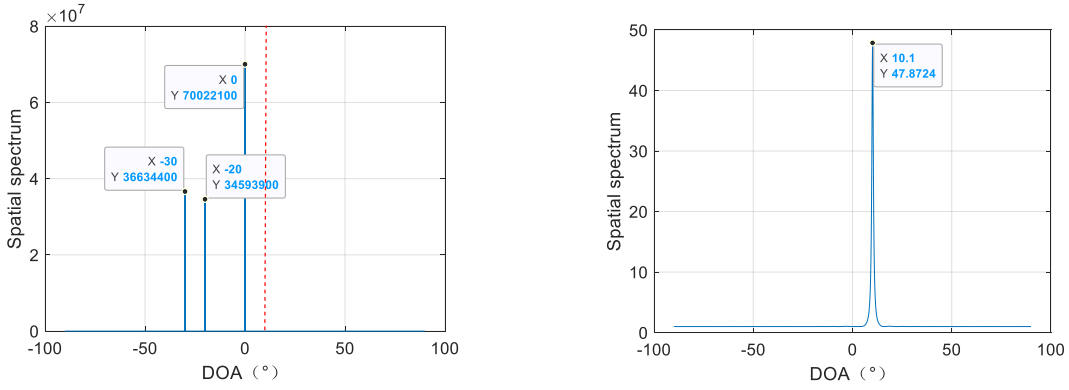


(a) (b)

Fig. 7. Target and interference located within the same beam range. (a) Before interference suppression. (b) After interference suppression.

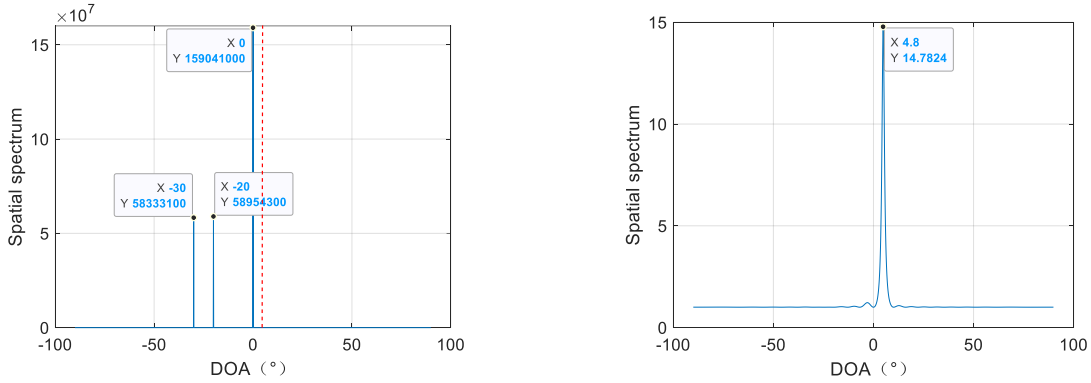
(2) Multiple DPIs and a reflected signal of target

In this analysis, it is assumed that the incident angle of the DPI is 0°, -20° and -30°, respectively. The INRs of the DPIs are 60 dB, 50 dB and 45 dB, respectively, while the SNR of the target is 0 dB. Fig. 8 illustrates the spatial spectrum curves before and after interference suppression using the proposed algorithm when the target angle is 10° (where the target and the interference/multipath clutters are outside the same beam range). Fig. 9 depicts the spatial spectrum curves before and after interference suppression using the proposed algorithm when the target angle is 4° (where the target and the interference/multipath clutters are within the same beam range). The red dashed lines in the figures indicate the direction of the target.



(a) (b)

Fig. 8. Target and interference located in separate beam ranges. (a) Before interference suppression. (b) After interference suppression.

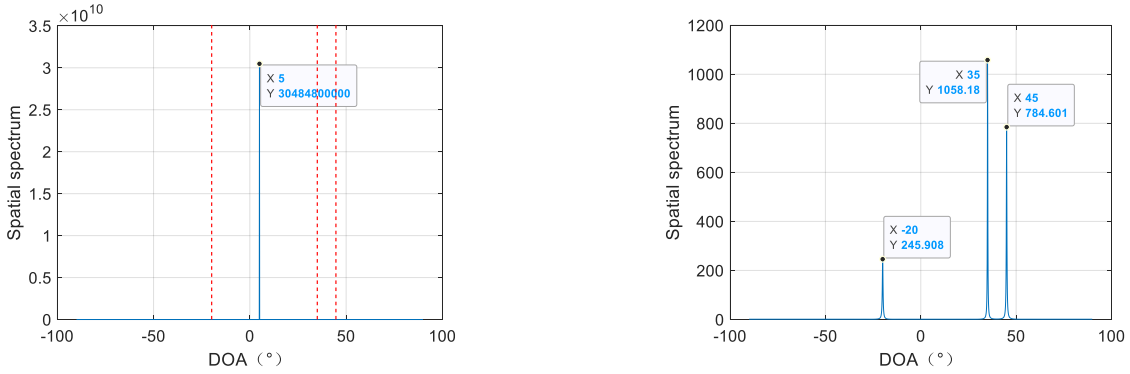


(a) (b)

Fig. 9. Target and interference located within the same beam range. (a) Before interference suppression. (b) After interference suppression.

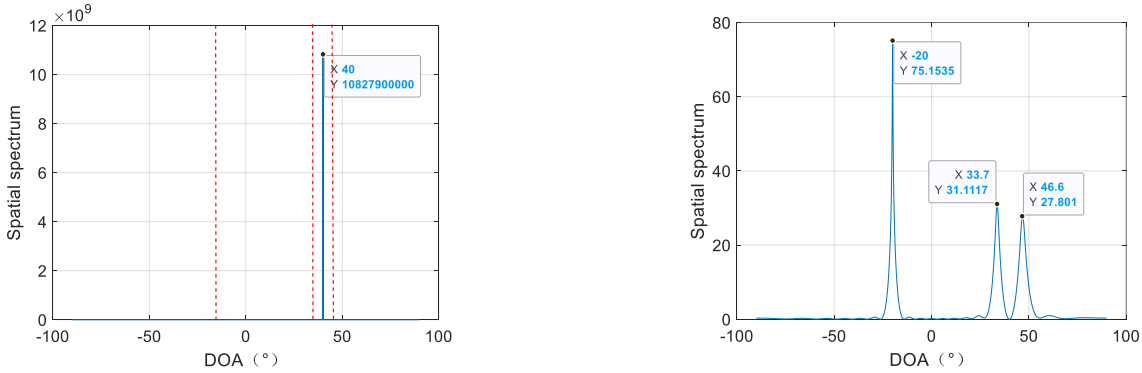
(3) A DPI and multiple reflected signals of targets

The analysis assumes three target reflected signals with angles of -20°, 35°, and 45°, and corresponding SNRs of 0 dB, 5 dB, and 10 dB, respectively, while the INR is set at 60 dB. Fig.10 depicts the spatial spectrum curves before and after interference suppression using the proposed algorithm when the interference incident angle is 5° (indicating that the targets and interference are outside the same beam range). Fig.11 shows the spatial spectrum curves before and after interference suppression using the proposed algorithm when the interference incident angle is 40° (indicating that the targets and interference are within the same beam range). The red dashed lines in the figures represent the directions of the targets.



(a) (b)

Fig. 10. Target and interference located in separate beam ranges. (a) Before interference suppression. (b) After interference suppression.



(a) (b)

Fig. 11. Target and interference located within the same beam range. (a) Before interference suppression. (b) After interference suppression.

From Fig. 6 to 11, it can be seen that in three typical scenarios, since the intensity of the DPI is much greater than that of the target reflected signal, the target reflected signal is submerged in strong interference and it is difficult to detect the target signal. However, by using the eigenvector elimination algorithm proposed in this paper, strong interference can be suppressed. In addition, when the target and DPI are not within the same beam range, the condition

of direction-preserving orthogonality of interference/target eigenvectors is satisfied, and the proposed algorithm can accurately estimate the DOA of the target, as shown in Fig.6(b), Fig.8(b), and Fig.10(b). When the target and DPI are within the same beam range, the condition of direction-preserving orthogonality of interference/target eigenvectors is not satisfied, and the target DOA estimated by the proposed algorithm has a large deviation, as shown in Fig.7(b), Fig.9(b), and Fig.11(b).

5.3. Statistical performance of DOA estimation for targets

The following three scenarios are set for non-cooperative bistatic radar operations: 1. One DPI and one target reflected signal, with DOA at -10° and 15°, respectively. 2. two DPIs and one target reflected signal, with DOAs at -10°, 35° and 15°, respectively. 3. One DPI and two target reflected signals, with DOAs at -10°, 15°, and 25°, respectively. Fig. 12 shows the comparison curves of the estimated deviation, Root Mean Square Error (RMSE), and success probability of the algorithm in this paper under three scenarios as a function of SNR. The results are the statistical results of 500 Monte-Carlo experiments (100 Monte-Carlo simulations are performed at each SNR point). During the simulation process, the INR is set to 60 dB, and the SNR changes from -20 dB to 10 dB in steps of 1 dB.

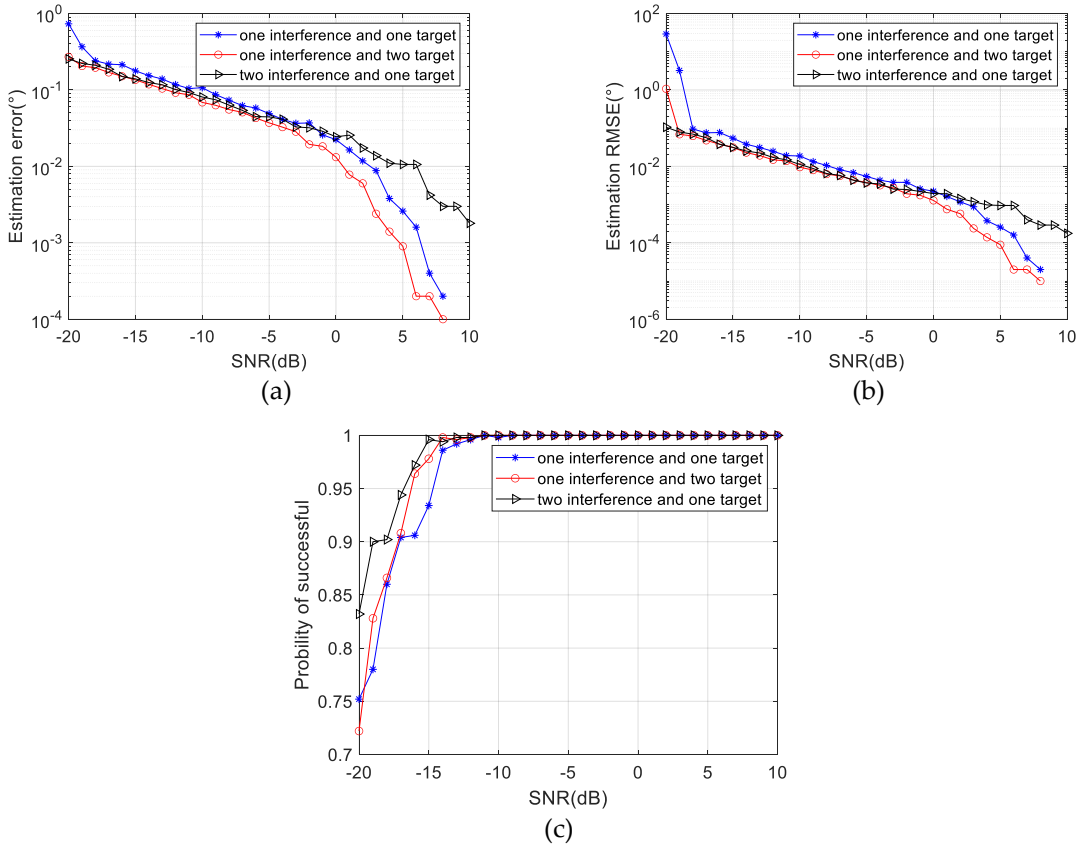


Fig. 12. Comparative performance curves of DOA estimation for target reflected signals in three scenarios using the proposed algorithm. (a) Estimation error, (b) Estimation RMSE, (c) Probability of successful.

From the Monte Carlo experimental results shown in Fig. 12, it can be observed that, regardless of the scenario, the DOA of the target can be accurately estimated by the proposed algorithm, provided that the conditions for direction-preserving orthogonality are satisfied. Furthermore, a high success rate is achieved even under low SNR conditions.

To further illustrate the superiority of the proposed algorithm, a comparative analysis is performed between the proposed algorithm and the existing CLEAN algorithm [38], JJM algorithm, the algorithm proposed in [39]. Fig.13 shows the comparison curves of estimation error, RMSE, and success probability as functions of SNR for the four algorithms. The results are based on 500 Monte Carlo experiments. In the simulations, it is assumed that one DPI and one target reflected signal are present. The DOA of the target reflected signal is set to 15°, with the SNR varying from -20 dB to 10 dB in steps of 1 dB. The DOA of the interference is set to -10°, and the INR is fixed at 60 dB.

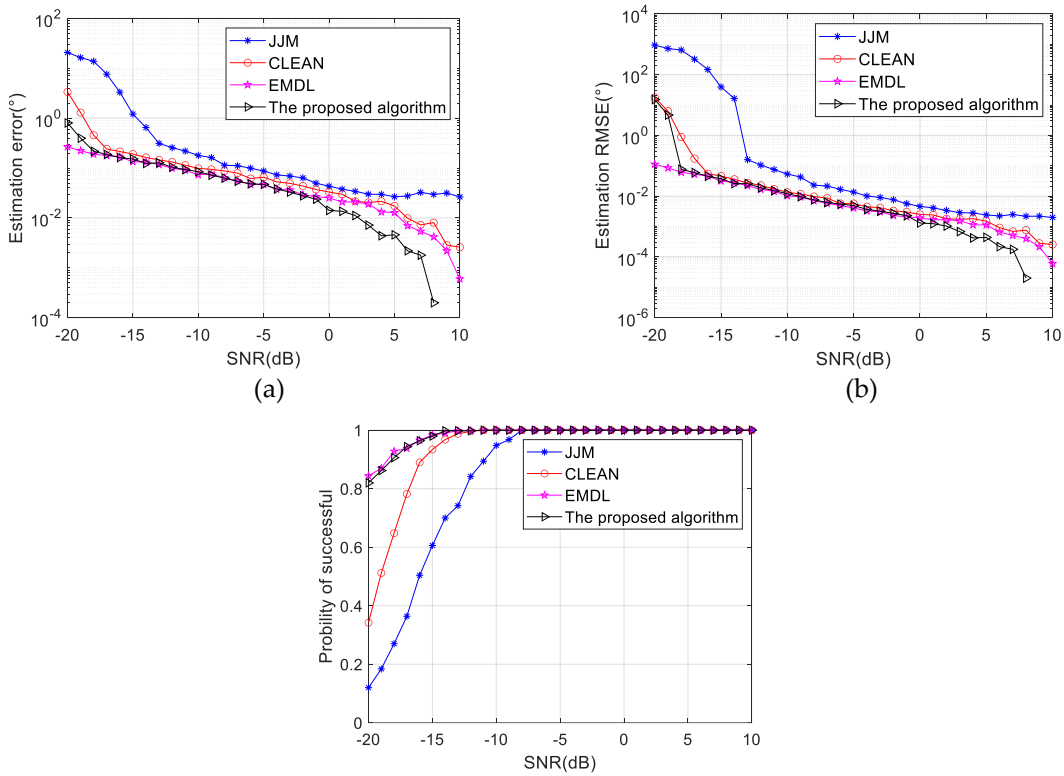


Fig. 13. Comparison of DOA estimation performance for target reflected signals among three algorithms. (a) Estimation error, (b) Estimation RMSE, (c) Probability of successful.

As shown in Fig.13, the proposed algorithm demonstrates a lower SNR resolution threshold, smaller estimation error, and reduced RMSE compared to the JJM and CLEAN algorithms, but it is almost the same as the algorithm in [39]. This indicates that the proposed algorithm is more effective in suppressing DPI.

6. Conclusions

In this work, we demonstrate, based on three typical scenarios of non-cooperative bistatic radar, that the eigenvectors of the interference and the target are direction-preserving orthogonal when the power of DPI and the target differ significantly and are not in the same beam range. On this basis, an algorithm for DPI suppression based on eigenvector rejection is proposed. In contrast to existed DPI suppression approaches, the proposed algorithm has the advantage of no need to predict the orientation of DPI and no need to set the RC, which is very useful for practical purposes. Several Monte Carlo simulation results have been to illustrate the conditions under which the direction-preserving orthogonality of interference and target eigenvectors holds and the performance of the proposed algorithm, and then compare it with the CLEAN algorithm, JJM algorithm and the algorithm proposed in [39]. The results show that the proposed algorithm can effectively suppress the DPI, and has better performance than the CLEAN and JJM algorithms when the conditions of the direction-preserving orthogonal are satisfied.

Future research track might encompass considering the scenarios with multiple interferences and multiple target signals and solve it based on proving that the interference and target signal eigenvectors are direction-preserving orthogonal.

Acknowledgements Not Applicable.

Author Contributions Yiduo Guo: Conceptualization, methodology, validation writing—original draft preparation. Jiawei Lu: Investigation, data curation, writing—review and editing. Yu Zhang: Supervision, funding acquisition.

Funding This work was supported in part by the Natural Science Foundation of Shaanxi Province under Grant No. 2025JC-YBQN-868.

Data Availability The data presented in this study are available from the corresponding author on reasonable request.

Declarations

Conflicts of Interest The authors declare no conflict of interest.

Appendix

A. Proof of Proposition 1

Let $x = \sigma_2^2 / \sigma_1^2$. Eq.7 and Eq.8 can be rewritten as follows

$$\lambda_2 = L\sigma_2^2 - \frac{\sigma_2^2\left(L(x-1)+\sqrt{L^2(1-x)^2+4v^2x}\right)}{2x} \tag{A1}$$

$$\left|\boldsymbol{a}_2^{\mathrm{H}}\boldsymbol{e}_2\right|^2 = \frac{L}{2} + \frac{L^2(1-x)-2v^2}{2\sqrt{L^2(1-x)^2+4v^2x}} \tag{A2}$$

However, as the power difference between the DPI and the target reflected signal increases, in the limiting case where $x \to 0$, applying L'Hôpital's rule yields

$$\lim_{x\to 0}\lambda_2 = L\sigma_2^2 - \frac{v^2\sigma_2^2}{L} \tag{A3}$$

$$\lim_{x\to 0}\left|\boldsymbol{a}_2^{\mathrm{H}}\boldsymbol{e}_2\right|^2 = L - \frac{v^2}{L} \tag{A4}$$

Based on Eq.6 and Eq.A4, the following can be obtained

$$\lim_{x\to 0}\left|\boldsymbol{a}_1^{\mathrm{H}}\boldsymbol{e}_2\right|^2 = 0 \tag{A5}$$

Eq.A4 and Eq.A5 indicate that as $x \to 0$, where the DPI and target reflected signals exhibit significant power differences, the eigenvector $\boldsymbol{e}_2$ corresponding to the target reflected signal is orthogonal to $\boldsymbol{a}_1$. However, whether it retains conservative orientation requires further analysis.

Substituting Eq.A3 into Eq.4 leads to

$$\boldsymbol{a}_1\boldsymbol{a}_1^{\mathrm{H}}\boldsymbol{e}_2 + x\boldsymbol{a}_2\boldsymbol{a}_2^{\mathrm{H}}\boldsymbol{e}_2 = \left(L - \frac{v^2}{L}\right)x\boldsymbol{e}_2 \tag{A6}$$

Let $x \to 0$, then: $\boldsymbol{a}_1\boldsymbol{a}_1^{\mathrm{H}}\boldsymbol{e}_2 = \boldsymbol{\theta}$.

From the perspective of simultaneously satisfying Eq.A6, it can be derived that

$$\boldsymbol{e}_2 = \left(\boldsymbol{I} - \frac{\boldsymbol{a}_1\boldsymbol{a}_1^{\mathrm{H}}}{L}\right)\boldsymbol{\delta} \tag{A7}$$

where $\boldsymbol{\delta}$ is an arbitrary vector that ensures $\boldsymbol{e}_2$ satisfies the normalization condition. From the standpoint of satisfying Eq.A5, it can be derived that

$$\boldsymbol{e}_2 = \frac{\left(\boldsymbol{I} - \frac{\boldsymbol{a}_1\boldsymbol{a}_1^{\mathrm{H}}}{L}\right)}{\sqrt{\left(L - \frac{v^2}{L}\right)}}\boldsymbol{a}_2 \tag{A8}$$

Thus, the proof is complete.

B. Proof of Proposition 2

When the power of the target reflected signal is significantly lower than that of the direct wave and multipath clutter, i.e., $\frac{\sigma_M^2}{\sigma_{M-1}^2} \to 0$, by substituting Eq.19 into Eq.16 and dividing both sides by the power of the target reflected signal, the following expression is obtained

$$\left(\frac{\boldsymbol{R}_{M-1}}{\sigma_{M-1}^2} + \frac{\sigma_M^2}{\sigma_{M-1}^2}\boldsymbol{a}_M\boldsymbol{a}_M^{\mathrm{H}}\right)\boldsymbol{e}_i = \left(\frac{\lambda_i'}{\sigma_{M-1}^2} + \frac{\sigma_M^2}{\sigma_{M-1}^2}\frac{\boldsymbol{e}_i'^{\mathrm{H}}\boldsymbol{a}_M\boldsymbol{a}_M^{\mathrm{H}}\boldsymbol{e}_i}{\boldsymbol{e}_i'^{\mathrm{H}}\boldsymbol{e}_i}\right)\boldsymbol{e}_i \tag{A9}$$

At this point, Eq.A9 can be rewritten as follows

$$\boldsymbol{R}_{M-1}\boldsymbol{e}_i = \lambda_i'\boldsymbol{e}_i \tag{A10}$$

Thus, it can be concluded that under the condition $\frac{\sigma_M^2}{\sigma_{M-1}^2} \to 0$, $\boldsymbol{e}_i = \boldsymbol{e}_i'$. Consequently, Eq.24 becomes

$$\lambda_M = L\sigma_M^2 - \sigma_M^2\sum_{i=1}^{M-1}\left|\boldsymbol{a}_M^{\mathrm{H}}\boldsymbol{e}_i\right|^2 \tag{A11}$$

Conversely

$$\sum_{i=1}^{M-1}\sigma_i^2\boldsymbol{a}_i\boldsymbol{a}_i^{\mathrm{H}}\boldsymbol{e}_M+\sigma_M^2\boldsymbol{a}_M\boldsymbol{a}_M^{\mathrm{H}}\boldsymbol{e}_M=\lambda_M\boldsymbol{e}_M \tag{A12}$$

Both sides are divided by σ_{M-1}^2, and Eq.A11 is then substituted in

$$\left(\frac{\sum_{i=1}^{M-1}\sigma_i^2\boldsymbol{a}_i\boldsymbol{a}_i^{\mathrm{H}}}{\sigma_{M-1}^2}+\frac{\sigma_M^2}{\sigma_{M-1}^2}\boldsymbol{a}_M\boldsymbol{a}_M^{\mathrm{H}}\right)\boldsymbol{e}_M=\left(L\frac{\sigma_M^2}{\sigma_{M-1}^2}-\frac{\sigma_M^2}{\sigma_{M-1}^2}\sum_{i=1}^{M-1}\left|\boldsymbol{a}_M^{\mathrm{H}}\boldsymbol{e}_i\right|^2\right)\boldsymbol{e}_M \tag{A13}$$

Since $\frac{\sigma_M^2}{\sigma_{M-1}^2}\to 0$, it can be concluded that

$$\sum_{i=1}^{M-1}\sigma_i^2\boldsymbol{a}_i\boldsymbol{a}_i^{\mathrm{H}}\boldsymbol{e}_M=0 \tag{A14}$$

It can be derived from Eq.50 that the following holds

$$\boldsymbol{e}_M=\left[\boldsymbol{I}-\boldsymbol{A}_{M-1}\left(\boldsymbol{A}_{M-1}^{\mathrm{H}}\boldsymbol{A}_{M-1}\right)^{-1}\boldsymbol{A}_{M-1}^{\mathrm{H}}\right]\boldsymbol{\delta} \tag{A15}$$

where $\boldsymbol{\delta}$ represents an arbitrary vector that satisfies the eigenvector normalization condition. However, it is known that $\boldsymbol{e}_M$ is unique. To determine $\boldsymbol{\delta}$, additional constraints must be imposed.

Multiply both sides of Eq.A12 by $\boldsymbol{e}_M^{\mathrm{H}}$ from the left, and substitute Eq.A11 into it, resulting in the following

$$\sum_{i=1}^{M}\sigma_i^2\left|\boldsymbol{a}_i^{\mathrm{H}}\boldsymbol{e}_M\right|^2=L\sigma_M^2-\sigma_M^2\sum_{i=1}^{M-1}\left|\boldsymbol{a}_M^{\mathrm{H}}\boldsymbol{e}_i\right|^2 \tag{A16}$$

Divide both sides by σ_M^2

$$\sum_{i=1}^{M-1}\frac{\sigma_i^2}{\sigma_M^2}\left|\boldsymbol{a}_i^{\mathrm{H}}\boldsymbol{e}_M\right|^2+\left|\boldsymbol{a}_M^{\mathrm{H}}\boldsymbol{e}_M\right|^2=L-\sum_{i=1}^{M-1}\left|\boldsymbol{a}_M^{\mathrm{H}}\boldsymbol{e}_i\right|^2 \tag{A17}$$

It can be inferred from Eq.A15 that

$$\left|\boldsymbol{a}_i^{\mathrm{H}}\boldsymbol{e}_M\right|^2=0,\ i=1,2,\ldots,M-1 \tag{A18}$$

Meanwhile

$$\left|\boldsymbol{a}_M^{\mathrm{H}}\boldsymbol{e}_M\right|^2=L-\sum_{i=1}^{M-1}\left|\boldsymbol{a}_M^{\mathrm{H}}\boldsymbol{e}_i\right|^2 \tag{A19}$$

That is, the choice of δ must satisfy Eq.A19.

If we select

$$\boldsymbol{e}_M=\alpha\left(\boldsymbol{I}-\boldsymbol{A}_{M-1}\left(\boldsymbol{A}_{M-1}^{\mathrm{H}}\boldsymbol{A}_{M-1}\right)^{-1}\boldsymbol{A}_{M-1}^{\mathrm{H}}\right)\boldsymbol{a}_M \tag{A20}$$

where α is a constant that ensures $\boldsymbol{e}_M$ satisfies the normalization condition. Therefore

$$\left|\boldsymbol{a}_M^{\mathrm{H}}\boldsymbol{e}_M\right|^2=\boldsymbol{a}_M^{\mathrm{H}}\boldsymbol{e}_M\boldsymbol{e}_M^{\mathrm{H}}\boldsymbol{a}_M=|\alpha|^2\left|\boldsymbol{a}_M^{\mathrm{H}}\left(\boldsymbol{I}-\boldsymbol{A}_{M-1}\left(\boldsymbol{A}_{M-1}^{\mathrm{H}}\boldsymbol{A}_{M-1}\right)^{-1}\boldsymbol{A}_{M-1}^{\mathrm{H}}\right)\boldsymbol{a}_M\right|^2 \tag{A21}$$

Since $\boldsymbol{e}_i'=\boldsymbol{e}_i$, it can be concluded that

$$\boldsymbol{A}_{M-1}\left(\boldsymbol{A}_{M-1}^{\mathrm{H}}\boldsymbol{A}_{M-1}\right)^{-1}\boldsymbol{A}_{M-1}^{\mathrm{H}}=\boldsymbol{E}_S'^{\mathrm{H}}\boldsymbol{E}_S'=\boldsymbol{E}_S^{\mathrm{H}}\boldsymbol{E}_S \tag{A22}$$

where $\boldsymbol{E}_S'=\left[\boldsymbol{e}_1',\boldsymbol{e}_2',\cdots,\boldsymbol{e}_{M-1}'\right]$, $\boldsymbol{E}_S=\left[\boldsymbol{e}_1,\boldsymbol{e}_2,\cdots,\boldsymbol{e}_{M-1}\right]$.

Substituting this into Eq.A20

$$\boldsymbol{e}_M=\alpha\left(\boldsymbol{I}-\boldsymbol{E}_S^{\mathrm{H}}\boldsymbol{E}_S\right)\boldsymbol{a}_M \tag{A23}$$

Substituting Eq.A23 into Eq.A21

$$\left|\boldsymbol{a}_M^{\mathrm{H}}\boldsymbol{e}_M\right|^2=|\alpha|^2\left|\boldsymbol{a}_M^{\mathrm{H}}\left(\boldsymbol{I}-\boldsymbol{E}_S^{\mathrm{H}}\boldsymbol{E}_S\right)\boldsymbol{a}_M\right|^2=|\alpha|^2\left(L-\sum_{i=1}^{M-1}\left|\boldsymbol{a}_M^{\mathrm{H}}\boldsymbol{e}_i\right|^2\right)^2 \tag{A24}$$

Given that $\alpha=\frac{1}{\sqrt{L-\sum_{i=1}^{M-1}\left|\boldsymbol{a}_M^{\mathrm{H}}\boldsymbol{e}_i\right|^2}}$, it is substituted into Eq.A21, resulting in

$$\boldsymbol{e}_M=\frac{\left(\boldsymbol{I}-\boldsymbol{A}_{M-1}\left(\boldsymbol{A}_{M-1}^{\mathrm{H}}\boldsymbol{A}_{M-1}\right)^{-1}\boldsymbol{A}_{M-1}^{\mathrm{H}}\right)\boldsymbol{a}_M}{\sqrt{L-\sum_{i=1}^{M-1}\left|\boldsymbol{a}_M^{\mathrm{H}}\boldsymbol{e}_i\right|^2}} \tag{A24}$$

It precisely satisfies Eq.A19 and is therefore valid.

References

1. W. Xiong, Y. Lu, J. Song and X. L. Chen, "A two-stage track-before-detect method for non-cooperative bistatic radar based on deep learning," Remote Sensing, vol.15, no.15, 1-22, 2023.
2. C. Fabiola, F. Francesca, and P. Debora, "Passive radar: Past, present, and future challenges," IEEE Aerospace and Electronic Systems Magazine, vol.38, no. 1, 54-69, 2023.
3. M. Malanowski, M. Zywek, M. Plotka, and K. Kulpa, "Passive bistatic radar detection performance prediction considering antenna patterns and propagation effects," IEEE Trans. on Geoscience and Remote Sensing, vol.60, 1-16, 2022.
4. F. Santi, I. Pisciottano, D. Cristallini, and D. Pastina, "Impact of rotational motion estimation errors on passive bistatic ISAR imaging via backprojection algorithm," IEEE Journal of Selected Topics in Applied Earth Observations and Remote Sensing, vol.17, 3345-3365, 2024.
5. C. Fabiola, "DVB-T-based passive forward scatter radar: inherent limitations and enabling solutions," IEEE Trans. on Aerospace and Electronic Systems, vol.57, no. 2, 1184-1104, 2020.
6. D. Park, G. H. Park, J. H. Park, J. H. Bang, D. Kim, and H. N. Kim, "Interference suppression for an FM-radio-based passive radar via deep convolutional autoencoder," IEEE Trans. on Aerospace and Electronic Systems, vol.60, no. 1, 106-118, 2024.
7. C. Sora, C. David, W. Peter, and S. Zhou, "Multistatic target tracking for passive radar in a DAB/DVB network: initiation," IEEE Trans. on Aerospace and Electronic Systems, vol.51, no. 3, 2460-2469, 2015.
8. F. Paolo, C. Fabiola, and L. Pierfrancesco, "Potentialities and challenges of WiFi-based passive radar," IEEE Aerospace and Electronic Systems Magazine, vol.27, no. 11, 15-26, 2012.
9. P. Krysik, P. Samczynski, M. Malanowski, L. Maslikowski, and K. S. Kulpa, "Velocity measurement and traffic monitoring using a GSM passive radar demonstrator," IEEE Aerospace and Electronic Systems Magazine, vol.27, no. 10, 43-51, 2012.
10. P. Samczynski, K. Abratkiewicz, M. Plotka, T. P. Zielinski, J. Wszolek, S. Hausman, P. Korbel, and A. Ksiezyk, "5G network-based passive radar," IEEE Trans. on Geoscience and Remote Sensing, vol.60, 1-16, 2022.
11. Z. Zeng, Z. Shi, Y. Zhou, Y. Chen and Y. Pan, "An improved pre-processing algorithm for resolution optimization in Galileo-based bistatic SAR," IEEE Access, vol. 7, 122972-122981, 2019.
12. Z. Zhang, Y. Zheng, L. Zheng, and P. Zhu, "Range resolution and sampling frequency trade-off for GPS passive radar," Journal of Systems Engineering and Electronics, vol.33, no.1, 28-37, 2022.
13. Z. Li, C. Huang, Z. Sun, H. An, J. Wu, and J. Yang, "BeiDou-based passive multistatic radar maritime moving target detection technique via space–time hybrid integration processing," IEEE Trans. on Geoscience and Remote Sensing, vol.60, 1-12, 2022.
14. C. Luca, D. Danilo, C. Riccardo, R. Fabio, and T. Luciano, "A cost-effective SDR platform for performance characterization of RFID tags," IEEE Trans. on Instrumentation and Measurement, vol.61, no.4, 903-911, 2012.
15. C. Stephen, "Passive radar with the KrakenSDR > Spot stuff with TV antennas and a software-defined radio," IEEE Spctrum, vol.59, no.11, 16-18, 2022.
16. B. Tuysuz, J. Urbina, and F. D. Lind, "Development of a passive VHF radar system using software-defined radio for equatorial plasma instability studies," Radio Science, vol.48, no.4, 416-426, 2013.
17. F. Nivole, C. Brousseau, S. Avrillon, D. Lemur, and L. Bertel, "Radio direction finding applied to DVB-T network for vehicular mobile reception," in 2009 3rd European Conference on Antennas and Propagation, Berlin, Germany, 2009.
18. T. Martelli, F. Colone and R. Cardinali, "Simultaneous short and long range surveillance of drones and aircrafts with DVB-T based Passive Radar," 2019 International Radar Conference (RADAR), Toulon, France, 2019, pp. 1-6.
19. D. Wang, Q. Bao, R. Tian, and Z. Chen, "Bistatic weak target detection method using non-cooperative air surveillance radar," Journal of Systems Engineering and Electronics, vol.26, no.5, 954-963, 2015.
20. Y. Zhang, "Adaptive clutter suppression method for non-cooperative detection radar," in 2019 IEEE International Symposium on Phase Array System and Technology, Waltham, MA, USA, 2019.
21. X. Guan, D. Hu, L. Zhong, and C. Ding, "Strong echo cancellation based on adaptive block notch filter in passive radar," IEEE Geoscience and Remote Sensing Letters, vol.12, no.2, 339-343, 2015.
22. J. Huang, M. Barr, J. Garry, and G. Smith, "Subarray processing for passive radar localization," in 2017 IEEE Radar Conference, Seattle, WA, USA, 2017.
23. M. Masjedi, M. Modarres-Hashemi, S. Sadri, "Direct path and multipath cancellation in passive radars using Subband Variable Step-Size LMS algorithm," in 2011 19th Iranian Conference on Electrical Engineering, Tehran, Iran, 2011.
24. M. Michal, "Cheap cancellation of strong echoes for digital passive and noise radars," IEEE Trans. on Signal Processing, vol.60, no.5, 2654-2659, 2012.
25. J. Park, J. Hong, J. Choi, and M. Hahn, "Determinant-based generalized sidelobe canceller for dual-sensor noise reduction," IEEE Sensors Journal, vol.22, no.9, 8858-8868, 2022.
26. X. Chen, T. Shu, K. Yu, J. He, and W. Yu, "Joint adaptive beamforming techniques for distributed array radars in multiple mainlobe and sidelobe jammings," IEEE Antennas and Wireless Propagation Letters, vol.19, no.2, 248-252, 2020.
27. J. Zhang, Z. Wang, J. Li, Q. Wu, W. Chen, and F. Shu, "How often channel estimation is required for adaptive IRS beamforming: A bilevel deep reinforcement learning approach," IEEE Trans. on Wireless Communications, vol.23, no.8, 8744-8759, 2024.
28. B. Liu, G. Gui, S. Y. Matsushita and L. Xu, "Compressive Sensing Based Direction-of-Arrival Estimation in MIMO Radars in Presence of Strong Jamming via Blocking Matrix," *2018 IEEE 10th Sensor Array and Multichannel Signal Processing Workshop (SAM)*, Sheffield, UK, 2018, pp. 292-296.

29. A. Mohamed, L. Toufik, A. Aladdine, and M. Ali, "Adaptive filters for direct path and multipath interference cancellation: Application to FM-RTL-SDR based passive bistatic radar," in 2016 7th International Conference on Sciences of Electronics Technologies of Information and Telecommunications, Hammamet, Tunisia, 2016.
30. X. Guan, L. Zhong, D. Hu, and C. Ding, "Adaptive direct signal and clutter cancellation based on phase-offset block least mean square filter in passive radar," in 2014 12th International Conference on Signal Processing, Hangzhou, China, 2014.
31. F. Colone, D. O'hagan, P. Lombardo, "A multistage processing algorithm for disturbance removal and target detection in passive bistatic radar," IEEE Trans. on Aerospace and Electronic Systems, vol.45, no.2, 698-722,2009.
32. F. Colone, C. Palmarini, T. Martelli, "Sliding extensive cancellation algorithm for disturbance removal in passive radar," IEEE Trans. on Aerospace and Electronic Systems, vol.52, no.3, 1309-1326, 2016.
33. B. Liu, G. Gui, S. Y. Matsushita and L. Xu, "Compressive sensing based direction-of-arrival estimation in MIMO radars in presence of strong jamming via blocking matrix," *2018 IEEE 10th Sensor Array and Multichannel Signal Processing Workshop (SAM)*, Sheffield, UK, 2018, pp. 292-296.
34. A. A. Salama and A. S. Abdel-Rahman, "Direct signal suppression in passive radar systems using beam-space processing," *2025 International Telecommunications Conference*, Cairo, Egypt, 2025, pp. 790-794.
35. H. Nikaein, R. G. Zefreh, and S. Gazor, "Target detection and interference cancellation in passive radar sensors via group-sparse regression," IEEE Sensors Journal, vol. 23, no. 18, 21484-21492, 2023.
36. X. D. Zhang, Matrix analysis and applications. Tsinghua University Press, China: Beijing, 2013.
37. A. Ghosh, A. K. Ray, and M. Jamshidi, "A Gershgorin circle theorem inspired controller for renewable energy source integrated power systems and multimicrogrids," IEEE Systems Journal, vol. 17, no. 3, 3858-3869, 2023.
38. Q. Niu, W. Shi, Q. Zhang and C. Zhang, "An improved CLEAN direct-wave suppression algorithm in integrated system of underwater detection and communication," IEEE Sensors Journal, vol. 24, no. 6, 8503-8516, 2024.
39. Q. Zhou, Y. Yuan, H. Li, M. S. Greco, F. Gini and W. Yi, "Direct localization with direct-path interference for reference channel-free distributed passive radars," IEEE Transactions on Signal Processing, vol. 73, 4379-4396, 2025.